

Dynamical Evidence for a Billion Solar Mass Black Hole in Galaxy NGC 4061 from ALMA $^{12}\text{CO}(2-1)$ Kinematics

DIEU D. NGUYEN ,¹ LONG Q. T. NGUYEN ,² ELENA GALLO ,¹ HAI N. NGO ,² QUE T. LE ,³ FABIO PACUCCI ,^{4,5} TINH Q. T. LE ,³
 TUAN N. LE ,² AND TIEN H. T. HO ,²

¹Department of Astronomy, University of Michigan, 1085 South University Avenue, Ann Arbor, MI 48109, USA

²Faculty of Physics—Engineering Physics, University of Science, Vietnam National University in Ho Chi Minh City, Vietnam

³Department of Physics, International University, Vietnam National University in Ho Chi Minh City, Vietnam

⁴Center for Astrophysics—Harvard & Smithsonian, 60 Garden St., Cambridge, MA 02138, USA

⁵Black Hole Initiative, Harvard University, 20 Garden St., Cambridge, MA 02138, USA

(Received January 26, 2026)

Submitted to AAS Journals

ABSTRACT

We present the first robust dynamical measurement of the supermassive black hole (SMBH) mass in the massive early-type galaxy NGC 4061 using high-spatial-resolution ALMA observations of the $^{12}\text{CO}(2-1)$ emission. By combining archival Cycle 6 data with new Cycle 7 observations, we achieve a synthesized beam of $0''.16 \times 0''.13$, comparable to the expected sphere of influence of the central black hole. The molecular gas forms a regularly rotating circumnuclear disk aligned with the prominent dust lane seen in HST imaging. We model the full three-dimensional ALMA data cube using the KinMS forward-modeling framework, exploring both data-driven and analytic prescriptions for the gas surface brightness distribution. Our Bayesian analysis yields a best-fitting SMBH mass of $M_{\text{BH}} = (1.17^{+0.08} \text{ [stat.]} \pm 0.43 \text{ [syst.]}) \times 10^9 \text{ M}_{\odot}$ and an I -band stellar mass-to-light ratio of $M/L_{\text{F814W}} = 3.46^{+0.07} \text{ [stat.]} \pm 0.10 \text{ [syst.] M}_{\odot}/\text{L}_{\odot}$. The inferred black hole mass is fully consistent across different modeling assumptions and remains insensitive to plausible radial variations in the M/L_{F814W} profile. Our results resolve the long-standing discrepancy between previous indirect mass estimates based on conflicting stellar velocity dispersion measurements and demonstrate that the exceptionally large dispersion reported in the literature is likely spurious. This study highlights the power of high-resolution ALMA molecular gas kinematics for precision SMBH mass measurements at the high-mass end of the local black hole mass function.

Keywords: Astrophysical black holes (98) — Galaxy kinematics (602) — Galaxy dynamics (591) — Interstellar medium (847) — Radio interferometry (1346) — Astronomy data modeling (1859)

1. INTRODUCTION

Supermassive black holes (SMBHs) are widely recognized as key drivers of galaxy formation and evolution (L. Ferrarese & D. Merritt 2000; N. J. McConnell & C.-P. Ma 2013; R. P. Saglia et al. 2016). This understanding is supported by well-established correlations between SMBH mass (M_{BH}) and large-scale host galaxy properties such as bulge luminosity (J. Magorrian et al. 1998) and stellar velocity dispersion (σ ; L. Ferrarese & D. Merritt 2000). These relations even have broader implications, for example: (i) constraining models of black hole (BH) fueling and feedback (J. Silk &

M. J. Rees 1998; A. C. Fabian 2012; H. Netzer 2015; T. Naab & J. P. Ostriker 2017), (ii) defining the SMBH mass function relevant for gravitational-wave background estimates for Pulsar Timing Arrays (L. Z. Kelley 2025) and space-based (LISA; J. Postiglione et al. 2025) detectors, and (iii) providing the calibration benchmark for reverberation-mapped active galactic nuclei (AGN) used to determine the virial factor in single-epoch M_{BH} estimations (A. E. Reines et al. 2013; J. E. Greene et al. 2024). Moreover, these local relations serve as a baseline for testing potential redshift evolution in the SMBH–galaxy connection (D. D. Nguyen et al. 2023, 2025a,b; F. Pacucci et al. 2023) and for constraining the nature of BH seeds at $z > 15$ (e.g., J. E. Greene et al. 2020a; K. Inayoshi et al. 2020).

However, these SMBH–host galaxy relations remain poorly constrained at both the low-mass ($M_{\text{BH}} \lesssim 10^6 \text{ M}_{\odot}$; D. D.

Corresponding author: Dieu D. Nguyen
 dieun@umich.edu

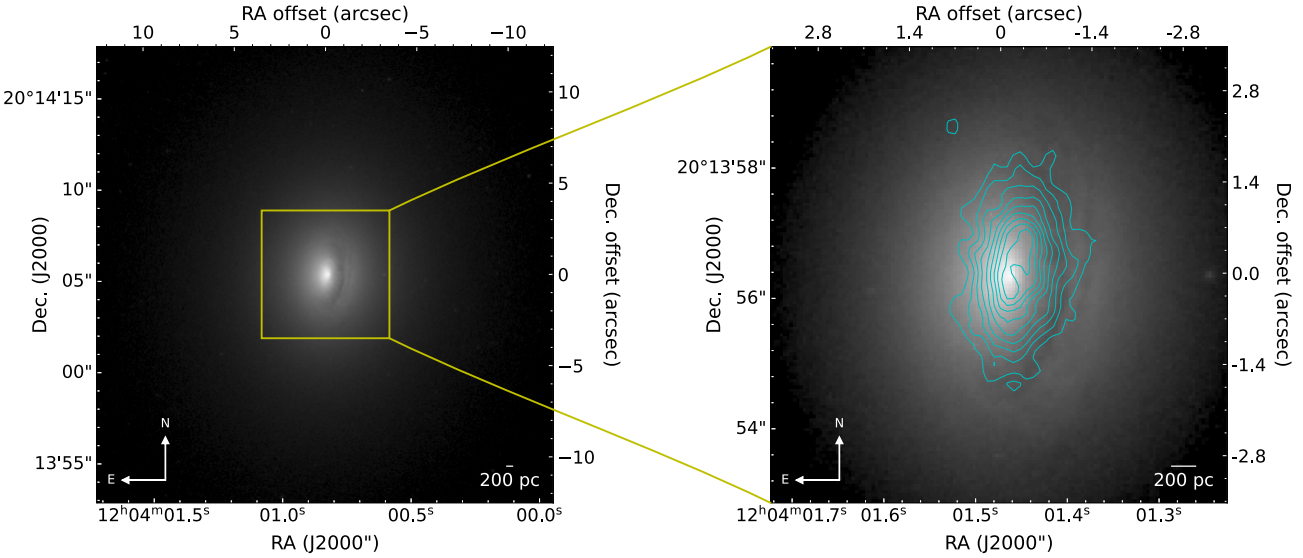


Figure 1. *Left:* HST/WFPC2 F814W image of NGC 4061 within a $25'' \times 25''$ (or 13 kpc \times 13 kpc) field of view, showing the central dust lane. *Right:* ALMA $^{12}\text{CO}(2-1)$ integrated intensity contours overlaid on the left zoom-in HST image ($7'' \times 7''$ or 3.64 kpc \times 3.64 kpc), illustrating the alignment of the molecular gas with the dust lane.

Nguyen et al. 2014; D. D. Nguyen 2017; D. D. Nguyen et al. 2025a) and high-mass ($M_{\text{BH}} \gtrsim 10^9 M_{\odot}$; J. Thomas et al. 2016; K. Mehrgan et al. 2019; J. W. Nightingale et al. 2023; C. R. Melo-Carneiro et al. 2025) ends. These relations are more complex than initially assumed, as galaxies with diverse structural properties (M. Cappellari 2016; A. W. Graham et al. 2025) and evolutionary histories—such as brightest cluster galaxies (N. J. McConnell et al. 2012; D. Krajnović et al. 2018), massive core ellipticals (N. J. McConnell et al. 2011; A. W. Graham & N. Scott 2013), compact early-type systems (A. C. Seth et al. 2014; D. D. Nguyen et al. 2017, 2018, 2019; C. P. Ahn et al. 2018; K. T. Voggel et al. 2018; M. A. Taylor et al. 2025), and low-mass spirals (M. den Brok et al. 2015; V. F. Baldassare et al. 2015; D. D. Nguyen et al. 2022)—exhibit notable deviations from the canonical scaling relations (J. Hlavacek-Larrondo et al. 2012; R. C. E. van den Bosch 2016a). To refine our understanding of the coevolution between SMBHs and their hosts, additional robust M_{BH} measurements are essential across the full mass spectrum and for a broad range of galaxy types (J. E. Greene et al. 2020b).

Located in the NGC 4065 group of galaxies, NGC 4061 (also catalogued as NGC 4055; R.A. = $12^{\text{h}}04^{\text{m}}01^{\text{s}}.4569$, Decl. = $+20^{\circ}13'56''.470$) has been studied primarily as a bent-tail radio source, whose morphology reflects its motion through the intragroup medium and interaction with the surrounding environment (S. M. Doe et al. 1995). These environmental signatures highlight both the richness of its dynamical context and the possibility that the central region may host significant kinematic complexity (E. Freeland et al. 2010). The galaxy thus presents an intriguing but underexplored laboratory for expanding the SMBH census toward the upper end of the mass distribution and for testing M_{BH} measurement techniques.

The Hypercat catalog lists an exceptionally large stellar velocity dispersion of $\sigma \approx 459$ km s $^{-1}$, implying an extremely massive BH ($M_{\text{BH}} \approx 1.2 \times 10^{10} M_{\odot}$) from the J. Kormendy & L. C. Ho (2013) relation. However, J. C. Pinkney & Nuker Team (2005) reported a much lower central dispersion of $\sigma \approx 290$ km s $^{-1}$, based on stellar kinematics derived long slit on the LDSS-3 instrument at the Magellan Clay telescope, suggesting a more moderate BH mass of $M_{\text{BH}} \approx 1.4 \times 10^9 M_{\odot}$ and indicating that the earlier value was likely overestimated. Additionally, optical observations from HST reveal a well-defined dust disk with a radius of $2''.5$ (left panel of Figure 1), while ground-based spectra show central H α emission from rapidly rotating gas, with a velocity gradient of 270 km s $^{-1}$ across $0''.55$ (J. C. Pinkney & Nuker Team 2005). This disk is nearly edge-on and closely aligned with the galaxy's projected major axis.

NGC 4061 is a massive early-type galaxy (ETG) at a distance of $D = 107.2$ Mpc, with an effective radius estimated in the range $R_e \sim 4.2\text{--}9.1$ kpc and a K -band absolute magnitude of $M_K = -25.3$ mag (C.-P. Ma et al. 2014). Using the prescription from equation (2) of M. Cappellari et al. (2013a), calibrated from 260 ATLAS^{3D} ETGs: $\log(M_{\star}) = 10.58 - 0.44 \times (M_K + 23)$, we estimate a stellar mass of $M_{\star} \approx 4.3 \times 10^{11} M_{\odot}$, placing NGC 4061 near the high-mass end of the $M_{\text{BH}}\text{--}\sigma$ relation and reinforcing the likelihood that it hosts a SMBH.

Despite these strong dynamical signatures, no published, peer-reviewed, high-precision M_{BH} measurement yet exists for NGC 4061. The geometry of its dust disk and the observed gas rotation provide a compelling case for high-spatial-resolution dynamical modeling (stellar or gas) to refine the mass estimate and test for systematic biases. Moreover, the

Table 1. Properties of ALMA observing tracks.

Project code	Obs. tracks	Obs. date	Config.	Baseline range	ToS	MRS	θ_{FWHM}	Calibration
(1)	(2)	(3)	(4)	(5)	(seconds)	(")	(")	Pipeline
					(6)	(7)	(8)	(9)
2018.1.00397.S	uid_A002_Xe03886_X7606	2019-08-19	C43-7	41.4 m–3.2 km	2780	1.6	0.112	CASA 5.4.0-70
	uid_A002_Xe03886_Xd75e	2019-08-20	C43-7	41.4 m–3.4 km	2805			
2019.1.00036.S	uid_A002_Xea90c0_X334e	2021-03-29	C43-5	15.0 m–1.3 km	3731	4.3	0.317	CASA 6.1.1.15

Notes: Columns: (2) Observational track ID. (3) Observational date (year-month-day). (4) ALMA configuration array. (5) Minimum and maximum baseline length. (6) Total on-source time (ToS). (7) Maximum recoverable scale (MRS), i.e. the largest angular scale that can be recovered with the given array. (8) the average synthesized beam size. (9) Calibration method.

Table 2. Properties of spectral windows of adopted observing tracks.

Project code	Obs. track	SPW	Target (Line)	Freq. range (GHz)	Cen. freq. (GHz)	Flagged	Bandpass (Quasars)	Phase (Quasars)
(1)	(2)	(3)	(4)	(5)	(6)	(7)	(8)	(9)
2018.1.00397.S	uid_A002_Xe03886_X7606	0	$^{12}\text{CO}(2-1)$	(224.09, 225.96)	225.0	No		
		1	cont.	(225.98, 227.97)	227.0	No	J1215+1654	J1157+1638
		2	cont.	(239.65, 241.63)	240.6	No		
		3	cont.	(241.56, 243.58)	242.6	No		
2018.1.00397.S	uid_A002_Xe03886_Xd75e	0	$^{12}\text{CO}(2-1)$	(224.09, 225.96)	225.0	No		
		1	cont.	(225.98, 227.97)	227.0	No	J1215+1654	J1157+1638
		2	cont.	(239.65, 241.63)	240.6	No		
		3	cont.	(241.56, 243.58)	242.6	No		
2019.1.00036.S	uid_A002_Xea90c0_X334e	0	cont.	(222.20, 224.07)	223.1	No		
		1	$^{12}\text{CO}(2-1)$	(224.19, 226.06)	225.1	No	J1058+0133	J1215+1654
		2	cont.	(236.12, 237.99)	237.1	No		
		3	cont.	(238.31, 240.19)	239.3	No		

Notes: Columns: (1) Project code. (2) Observational track ID. (3) SPW ID. (4) Targeted line of each SPW. (5) Frequency range of each SPW. (6) Central frequency of each SPW. (7) Whether the SPW is flagged manually. (8)–(9) Quasars used to do bandpass and phase calibration.

Table 3. Parameters of the 1.3 mm combined continuum image and source.

Image property	Value
Image size (pixel 2)	512 \times 512
Image size (arcsec 2)	20.5 \times 20.5
Image size (kpc 2)	10.7 \times 10.7
Pixel scale (arcsec per pixel)	0.04
Pixel scale (pc per pixel)	20.8
Sensitivity (mJy per beam)	0.02
Synthesised beam (arcsec 2)	0.16 \times 0.13
Synthesised beam (pc 2)	83.2 \times 67.6
Source property	Value
Right ascension	12 ^h 04 ^m 01 ^s .4569
Declination	+20°13'56.470
Integrated flux (mJy)	3.48 \pm 0.18
Deconvolved size (arcsec 2)	(0.26 \pm 0.03) \times (0.22 \pm 0.03)
Deconvolved size (pc 2)	(135.2 \pm 15.6) \times (114.4 \pm 15.6)

galaxy's group environment, bent-tail radio morphology, and

Table 4. The combined $^{12}\text{CO}(2-1)$ data cube properties

CO image property	Value
Spatial extent (pixel 2)	512 \times 512
Spatial extent (arcsec 2)	20.5 \times 20.5
Spatial extent (kpc 2)	10.7 \times 10.7
Pixel scale (arcsec per pixel)	0.04
Pixel scale (pc per pixel)	20.8
Velocity range (km s $^{-1}$)	6815 – 7550
Channel width (km s $^{-1}$)	10
Number of constraints	78,100
Mean synthesised beam (arcsec 2)	0.16 \times 0.13
Mean synthesised beam (pc 2)	83.2 \times 67.6
Sensitivity (mJy per beam per 10 km s $^{-1}$)	0.4

Notes: Assumed center of the $^{12}\text{CO}(2-1)$ circumnuclear disk, coincident with the 1.3 mm continuum emission described in Table 3.

potential AGN activity underscore the importance of linking central BH growth with its environmental and structural context.

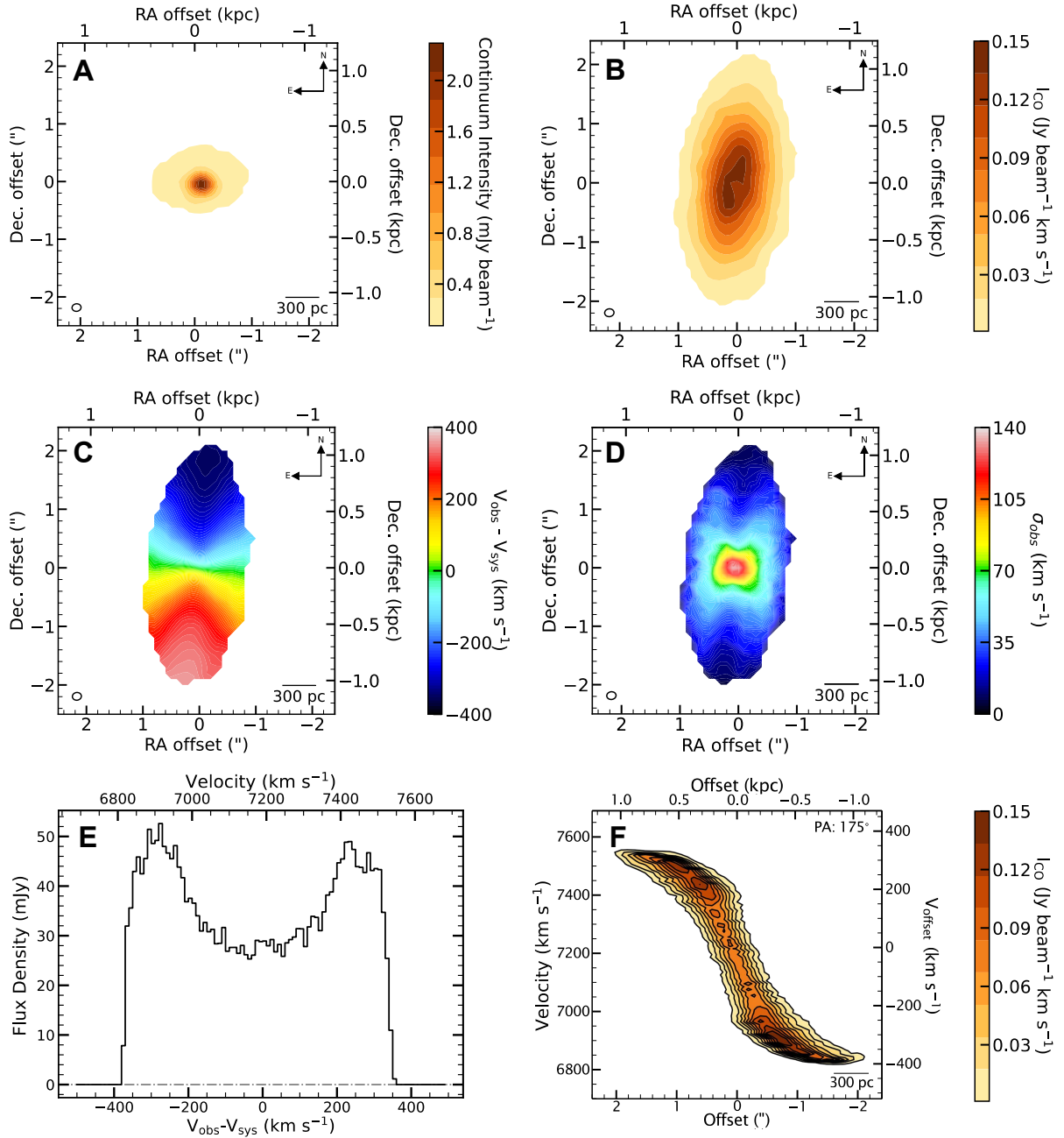


Figure 2. Panel A: 1.3 mm continuum emission in Band 6. Panels B–D: ALMA $^{12}\text{CO}(2-1)$ moment maps of NGC 4061—integrated intensity, intensity-weighted mean LOS velocity, and intensity-weighted LOS velocity dispersion, respectively. The synthesized beam is shown as a black ellipse in the lower-left corner of each map. Panel E: Integrated spectrum extracted from a $6'' \times 6''$ (3.12 \times 3.12 kpc) box; the horizontal dot-dashed line marks zero flux. Panel F: Position–velocity diagram along the major axis, adopting a systemic velocity of $v_{sys} = 7190$ km s⁻¹ and position angle $\Gamma = 175^\circ$.

In this work, we present new high-sensitivity, high-spatial-resolution observations of the $^{12}\text{CO}(2-1)$ circumnuclear disk (CND) in the central region of NGC 4061 obtained with the Atacama Large Millimeter/submillimeter Array (ALMA). These data allow us to map the cold molecular gas kinematics and, for the first time, to dynamically constrain the mass of its central SMBH precisely.

In Section 2, we describe the ALMA observations, data reduction, imaging, light-of-sight (LOS) kinematic measurements, and molecular gas mass derivation from the $^{12}\text{CO}(2-1)$ molecular gas. Section 3 presents the stellar mass modeling of NGC 4061 based on HST data, respectively. The molecular gas dynamical modeling used to measure M_{BH} and assess associated uncertainties are detailed in Section 4, followed by conclusions in Section 5. Given our adopted flat

Λ CDM cosmological model with $H_0 = 70 \text{ km s}^{-1} \text{ Mpc}^{-1}$, $\Omega_{\Lambda,0} = 0.7$, and $\Omega_{\text{m},0} = 0.3$, and a distance of $D = 107.2 \text{ Mpc}$ (C.-P. Ma et al. 2014), the physical scale is $520 \text{ pc } ''^{-1}$.

2. ALMA OBSERVATIONS

2.1. Data Reduction

We used the ALMA $^{12}\text{CO}(2-1)$ circumnuclear disk (CND) observations of NGC 4061 obtained during Cycles 6 (PID: 2018.1.000397.S; PI: M. Smith) and 7 (PID: 2019.1.00036.S; PI: D. Nguyen). The data were taken with the 12-m array in the C43-7 and C43-5 configurations, respectively, providing a primary-beam full width at half maximum (FWHM) of $\approx 25''$. A summary of these observing tracks is given in Table 1.

For each execution block, the observations were carried out in Band 6 using four frequency-division-mode (FDM) spectral windows (SPWs). Each SPW spans 2 GHz and is divided into 1920 channels (976.562 kHz, corresponding to $\approx 1.3 \text{ km s}^{-1}$). One SPW was centered on the $^{12}\text{CO}(2-1)$ transition ($v_{\text{rest}} = 230.538 \text{ GHz}$), while the remaining three SPWs were allocated to measure the continuum. The detailed spectral setup is listed in Table 2.

Calibration was carried out using the Common Astronomy Software Applications package, CASA⁶ (J. P. McMullin et al. 2007), with version 5.4.0-70 for the Cycle 6 data and version 6.1.1.15 for the Cycle 7 data. All datasets were processed using the standard ALMA Science Pipeline⁷ to obtain three measurement sets (MS) for three observational tracks listed in Tables 1 and 2.

We combined the visibility data from all three MS into a combined and calibrated MS using the `concat` task in CASA. The optimal visibility-weight scaling factors applied in the `visweightscale` mode were 0.6 for the `uid_A002_Xea90c0_X334e` MS (2019.1.00036.S), and 0.2 for each of the `uid_A002_Xe03886_X7606` and `uid_A002_Xe03886_Xd75e` MSs (2018.1.00397.S).

2.2. Creating the Combined 1.3 mm Continuum Image

We produced the combined continuum image at 1.3mm using the CASA `tclean` task in multifrequency synthesis mode (U. Rau & T. J. Cornwell 2011), combining the continuum SPWs with line-free channels from the targeted SPWs of all three MS. Briggs weighting with a robust parameter of 0.5 was applied to optimize the balance between sensitivity and resolution. The resulting image shows a resolved source with a size of $1''.8 \times 1''.2$ that has an RMS noise of $\sigma_{\text{cont}} = 120 \mu\text{Jy beam}^{-1}$ and a synthesized beam of $\theta_{\text{FWHM,cont}} = 0''.16 \times 0''.13$ at a position angle of $\Gamma = 352.9^\circ$.

Figure 2 (Panel A) displays the continuum image, showing a single source that matches the galaxy's kinematic center

Table 5. Gas MGE model

j	$\lg \Sigma_{\text{ISM},j} (\text{M}_\odot \text{ pc}^{-2})$	$\lg \sigma_j (")$	$q_j = b_j/a_j$
(1)	(2)	(3)	(4)
1	1.98	-0.23	0.94
2	2.71	-0.09	0.50
3	1.17	0.32	1.00

Notes: (1) the Gaussian component, (2) the luminosity surface density, (3) the Gaussian dispersion along the major axis, and (4) the axial ratio.

(best-fitting SMBH position; see Section 4.3, and also defined as the galaxy center), with an integrated flux density of $3.48 \pm 0.18 \text{ mJy}$, consistent within the $\approx 10\%$ ALMA flux calibration uncertainty. A two-dimensional (2D) Gaussian fit using the `imfit` routine in CASA confirms the source is spatially resolved. Continuum image parameters and source properties are summarized in Table 3.

2.3. Creating the Combined- $^{12}\text{CO}(2-1)$ Data Cube

Given that the 1.3 mm continuum emission is detected at the nucleus of NGC 4061 and is spatially resolved in all three MSs summarized in Table 2, we used the combined and calibrated MS (Section 2.1) with all line-free channels across the 12 targeted SPWs (Table 2). The continuum was modeled with a linear power-law function and subtracted from the combined and calibrated visibilities in the uv plane to isolate the $^{12}\text{CO}(2-1)$ line emission. This subtraction was carried out using the CASA task `uvcontsub` (e.g., T. A. Davis et al. 2020; D. D. Nguyen et al. 2020).

We produced the final three-dimensional (R.A., Decl., velocity) cube using the `tclean` task in CASA. To model the $^{12}\text{CO}(2-1)$ CND, constrain the mass of the central compact object, and optimize the balance between surface-brightness sensitivity and spatial resolution, we adopted a Högbom deconvolver (J. A. Högbom 1974). The resulting cube has dimensions of $512 \times 512 \text{ pixels}^2$ with a pixel scale of $0''.04$, which adequately samples the synthesized beam while maintaining a manageable file size. We used a channel width of 10 km s^{-1} —an optimal choice for SMBH dynamical modeling (T. A. Davis 2014; D. D. Nguyen et al. 2021; H. N. Ngo et al. 2025)—and Briggs weighting with a robust parameter of 0.5. The velocity axis was referenced to the rest frequency of 230.538 GHz.

During interactive imaging, we applied a clean mask to suppress sidelobe artifacts and improve the fidelity of the recovered emission. The continuum-subtracted dirty cube was cleaned down to a threshold of 1.5 times the root-mean-squared (RMS) noise level (σ_{RMS} ; measured from line-free channels). The final self-calibrated, cleaned cube shares the same synthesized beam as the 1.3 mm continuum image (Section 2.2), and its properties are summarized in Table 4.

⁶ <https://casa.nrao.edu/>

⁷ <https://almascience.eso.org/processing/science-pipeline>

2.4. $^{12}\text{CO}(2-1)$ Emission Moment Maps

The $^{12}\text{CO}(2-1)$ emission spans in a velocity range of 6815–7550 km s $^{-1}$, with a systemic velocity of $v_{\text{sys}} \approx 7190$ km s $^{-1}$. Moment maps, including the zeroth (integrated intensity; panel B), the first (intensity-weighted mean light-of-sight (LOS) velocity; panel C), and the second (intensity-weighted LOS velocity dispersion; panel D), were derived from the $^{12}\text{CO}(2-1)$ data cube using the masked-moment method (T. M. Dame 2011), as shown in Figure 2.

We first produced a smoothed version of the original data cube by duplicating it and applying a Gaussian spatial convolution with $\sigma = 1.5 \times \theta_{\text{FWHM}}$ and spectral smoothing with a Hanning window four times the channel width (M. D. Smith et al. 2021; P. Dominiak et al. 2024) to that copy of the original data cube. A mask was then generated by applying a $0.5\sigma_{\text{RMS}}$ threshold to the unsmoothed cube (equivalent to $8\sigma_{\text{RMS}}$ in the smoothed cube). This method effectively suppresses noise while retaining most of the flux. Pixels that exceed the threshold in the smoothed cube (or the mask) were used to create moment maps from the unsmoothed cube.

The zeroth-moment map shows that the CND extends $\approx 4''$ along the major axis and $2''$ along the minor axis, featuring a smooth intensity gradient and peaks at the CND’s center. Its also illustrates the alignment between the $^{12}\text{CO}(2-1)$ emission and the dust disk (see Figure 1). The total molecular gas mass was estimated by using the “CO-to-H₂ conversion factor” of $X_{\text{CO}} = 2 \times 10^{20} \text{ cm}^{-2} (\text{K km s}^{-1})^{-1}$ (or $\alpha_{\text{CO}} = 4.3 \text{ M}_{\odot} (\text{K km s}^{-1} \text{ pc}^{-1})^{-1}$; A. D. Bolatto et al. 2013):

$$M_{\text{gas}} = 1.05 \times 10^4 \left(\frac{X_{\text{CO}}}{2 \times 10^{20} \frac{\text{cm}^{-2}}{\text{K km s}^{-1}}} \right) \left(\frac{1}{1+z} \right) \left(\frac{S_{\text{CO}} \Delta v}{\text{Jy km s}^{-1}} \right) \left(\frac{D_L}{\text{Mpc}} \right)^2,$$

where $S_{\text{CO}} \Delta v = 4.2 \text{ Jy km s}^{-1}$ is the integrated flux density derived from our data cube. For NGC 4061 ($z \approx 0.024450$; NASA/IPAC Extragalactic Database⁸), we adopted a luminosity distance of $D_L = 107.2$ Mpc (C.-P. Ma et al. 2014) and a flux density ratio of unity between $^{12}\text{CO}(2-1)$ and $^{12}\text{CO}(1-0)$ (M. D. Smith et al. 2021). Under these assumptions, the total molecular gas mass is $M_{\text{gas}} \approx 4.95 \times 10^8 \text{ M}_{\odot}$.

The first-moment map shows a regularly intensity-weighted mean LOS rotating, unwarped thin disk with velocities up to ± 370 km s $^{-1}$. The second-moment map indicates moderate turbulence, with a gradient in the intensity-weighted LOS velocity dispersion of $0 \lesssim \sigma_{\text{LOS}} \lesssim 70$ km s $^{-1}$ outside the central boxy region ($0''.5 \times 0''.5$). Within this region, σ_{LOS} rises to ≈ 140 km s $^{-1}$ at the center, likely due to beam smearing and projection effects from the highly inclined disk (i.e., inclination angle of $i \gtrsim 50^\circ$). These joining effects results an “X”-shaped structure (T. A. Davis et al. 2017) at

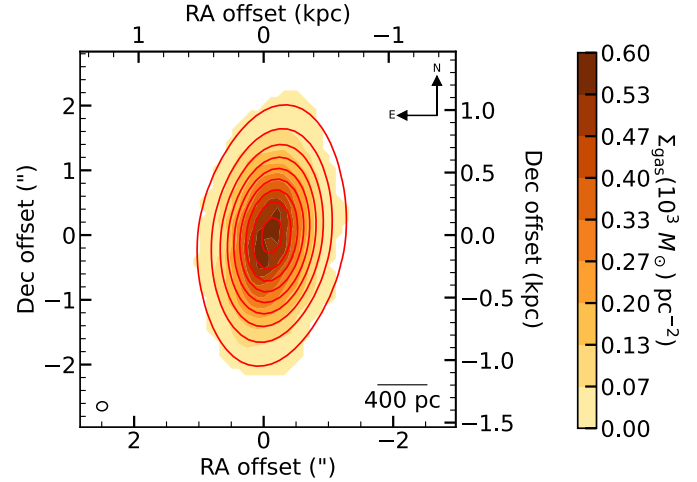


Figure 3. Comparison between the molecular gas mass distribution derived from the zeroth-moment map (panel B of Figure 2) and its MGE model (contours). The strong correspondence between the data and model demonstrates excellent agreement across matching radii and contour levels.

Table 6. MGE PSF model of HST/WFPC2 F814W image

j	$(\text{Light fraction})_j$	σ_j (arcsec)	$q'_j = b_j/a_j$
(1)	(2)	(3)	(4)
1	0.502	0.020	1.000
2	0.287	0.070	1.000
3	0.075	0.189	1.000
4	0.085	0.415	1.000
5	0.051	0.990	1.000

Notes. Same as Table 5 with column 2 lists the light fraction of each Gaussian.

Table 7. HST/WFPC2 F814W MGE model

j	$\lg \Sigma_{\star,j}$ ($\text{L}_{\odot} \text{ pc}^{-2}$)	$\lg \sigma_j$ ('')	$q'_j = b_j/a_j$
(1)	(2)	(3)	(4)
1	3.937	-0.396	0.857
2	3.662	-0.162	0.857
3	3.367	0.095	0.857
4	3.171	0.309	0.814
5	2.928	0.569	0.814
6	2.355	0.978	0.814
7	0.894	1.385	0.832

Notes: Same as Table 5.

the second-moment map’s center, reflecting steep intensity gradients across the beam (A. J. Barth et al. 2016; M. Kepler et al. 2019). As shown in Section 4.4, the best-fitting dynamical models yield an intrinsic velocity dispersion of 18–22 km s $^{-1}$, implying that beam smearing dominates the observed linewidths across most of the $^{12}\text{CO}(2-1)$ CND.

⁸ NED: <https://ned.ipac.caltech.edu>

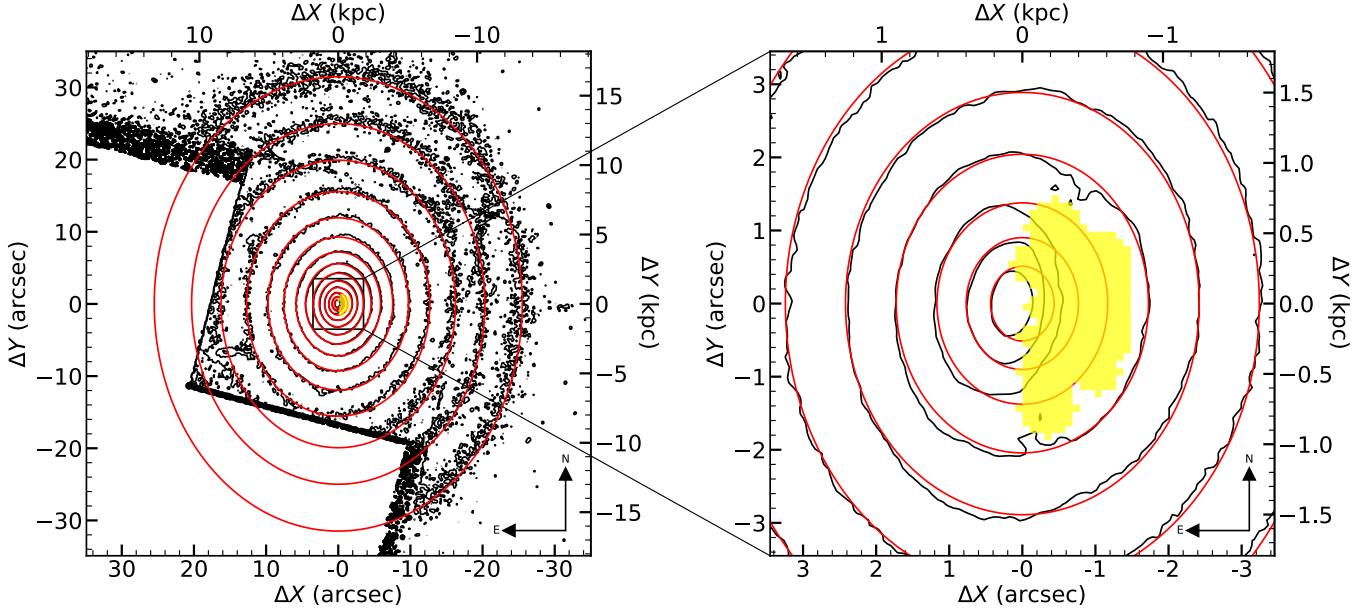


Figure 4. Comparison between the HST/WFPC2 F814W image and its MGE model, shown in 2D surface brightness density over the field of $70'' \times 70''$ (left) and a central zoom ($7'' \times 7''$; right). Black contours indicate the data, and red contours show the model, demonstrating close agreement across radii and contour levels. The yellow region marks masked areas affected by bad pixels and the central dust disk.

2.5. Interstellar Medium (ISM) Mass Model

To include the molecular gas mass ($M_{\text{gas}} \approx 4.95 \times 10^8 M_{\odot}$) in the dynamical estimation of M_{BH} , we modeled its mass distribution using the Multi-Gaussian Expansion (MGE⁹) algorithm (E. Emsellem et al. 1994), implemented via the PYTHON routine `mge_fit_sectors_regularized` (M. Capellari 2002a). This approach has been well tested in molecular gas modeling for dynamical BH mass measurements in NGC 3593 (D. D. Nguyen et al. 2022) and NGC 7052 (H. N. Ngo et al. 2025) with ALMA observations.

The zeroth-moment $^{12}\text{CO}(2-1)$ map (panel B of Figure 2) was converted into a molecular gas mass map and decomposed into multiple Gaussian components. This MGE decomposition was performed without deconvolving the synthesized beam, as the observational resolution had already been accounted for in the moment map creation. The resulting MGE parameters are listed in Table 5 and were fixed in the total mass model of NGC 4061 (i.e., with no free parameters). The good agreement between the data and the ISM MGE model is shown in Figure 3, where both are compared at identical contour levels of molecular gas-mass surface density.

Given the compactness of the continuum emission as seen in panel A of Figure 2, much smaller than the $^{12}\text{CO}(2-1)$ CND, and the negligible dust mass inferred from the HST optical image, we excluded the dust component from the total mass model.

⁹ v6.0.4: <https://pypi.org/project/mgefit/>

2.6. Integrated Spectrum & Position-Velocity Diagram

Panel E of Figure 2 shows the integrated $^{12}\text{CO}(2-1)$ spectrum of NGC 4061, extracted from a $6'' \times 6''$ ($3.12 \times 3.12 \text{ kpc}^2$) aperture enclosing all line emission. The spectrum exhibits a characteristic double-horn profile, indicative of a spatially resolved rotating disk. The nearly symmetric redshifted and blueshifted sides suggest a well-settled, regularly rotating CND.

Panel F shows the major-axis position–velocity diagram (PVD) extracted along the kinematic major axis of the CND (i.e., along the best-fitting position angle determined in Section 4.4; $\Gamma \approx 175^\circ$). The PVD was generated using a 2-pixel-wide ($0''.158$) pseudo-slit, applying a spatial Gaussian filter with a FWHM equal to the synthesized beam and selecting pixels above $0.5\sigma_{\text{RMS}}$ in the unsmoothed data cube. The diagram reveals a mild central rise in the intensity-weighted mean LOS velocity within the inner $\approx 0''.2$. The CND also traces an extended ($\approx 2''$) $^{12}\text{CO}(2-1)$ kinematics, providing tighter constraints on M/L and, consequently, on M_{BH} in our dynamical models.

3. GALAXY MASS MODEL

3.1. HST Imaging and Photometric Model

We used HST/WFPC2 F814W and F555W imaging of NGC 4061 (Program ID: 9106; PI: Douglas Richstone), obtained on May 26, 2001, with a total exposure time from four individual exposures of 1600 s for both F814W and F555W. The data were retrieved from the Hubble Legacy Archive

(HLA¹⁰). In our fiducial analysis, we construct the stellar mass model using the HST/F814W image, and we use the F555W image to evaluate the systematic uncertainty associated with adopting an alternative photometric band in our SMBH mass measurement (see Section 4.5.7).

We estimated the sky backgrounds for these two images by taking the median value from several 20×20 pixel² boxes located in source-free regions beyond $40''$ from the galaxy center and subtracting this median from the entire images to produce sky-subtracted frames.

To ensure accurate photometric modelings, we generated the HST/WFPC2 point spread functions (PSFs) for the F814W and F555W filters using the TINYTIM¹¹ package (J. E. Krist et al. 2011). Model PSFs of each filter were created for each of the four exposures based on the instrument configuration, chip position, and dither offsets, matching the original four-point box dither pattern. For each filter, the individual PSFs were convolved with the appropriate charge-diffusion kernel to account for CCD electron leakage. The four PSFs for each filter were then combined and resampled to a final pixel scale of $0''.1$ using Drizzlepac/ASTRODRIZZLE¹² (R. J. Avila et al. 2012).

A mask excluding the central dust lane, bad/hot pixels, and foreground stars was created for F814W (and similar to F555W) using a point-source catalog generated with SExtractor¹³ (E. Bertin & S. Arnouts 1996).

We derived the stellar light distribution from the sky-subtracted, masked F814W image using the MGE method described in Section 2.5. An alternative model based on the masked F555W image is presented in Section 4.5.7. For the F814W photometric calibration, we adopted a zero point of 24.204 mag, computed from the PHOTFLAM and PHOTPLAM keyword in the image header following the procedures outlined in the WFPC2 Data Handbook.¹⁴ We further assumed an *I*-band solar absolute magnitude of 4.52 mag (C. N. A. Willmer 2018), with all magnitudes expressed in the AB system. The fit was deconvolved using the HST/WFPC2 F814W TINYTIM PSF. The PSF was first decomposed into an MGE representation with the `mge_fit_sectors` routine (M. Cappellari 2002a) and is provided in Section 6. This MGE PSF was then used as input for the final MGE fit of the F814W image with `mge_fit_sectors_regularized`, yielding a set of 2D Gaussian components convolved with the PSF MGE. The resulting deconvolved MGE can be analytically deprojected into a three-dimensional (3D) axisymmetric light distribution

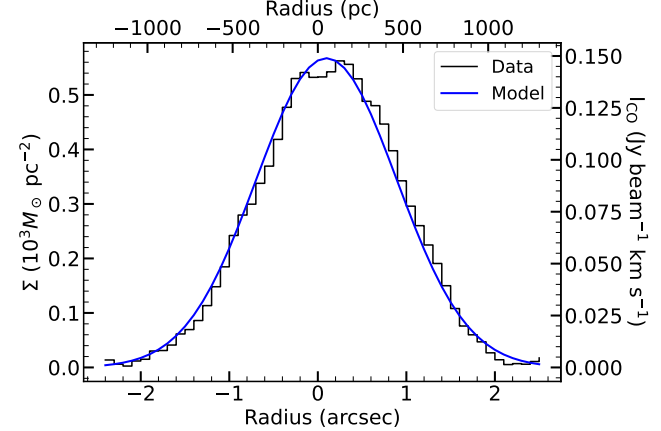


Figure 5. The $^{12}\text{CO}(2-1)$ -CND surface brightness distribution of NGC 4061 is best described by a simple Gaussian model. The ALMA data are plotted in black, and the model is overlaid in blue.

for an assumed inclination. The final MGE parameters are listed in Table 7 and compared with the F814W image in Figure 4.

3.2. Galaxy Mass Model

We converted the deconvolved light-MGE into a stellar mass model for NGC 4061 by adopting a constant mass-to-light ratio parameter (from the best-fit value in Section 4.4) and neglecting the dark matter contribution in the central region (M. Cappellari et al. 2013b), given the compact extent of the $^{12}\text{CO}(2-1)$ disk. The total mass model for NGC 4061 therefore consists of three components: a central point mass representing the SMBH, the stellar mass, and the ISM mass. This combined model is used to compute the circular velocity curve for the $^{12}\text{CO}(2-1)$ CND arising from the gravitational potential of these components.

4. DYNAMICAL MODELLING

4.1. *KinMS* Tool

We modeled the ALMA $^{12}\text{CO}(2-1)$ -CND kinematics of NGC 4061 for its central M_{BH} using the PYTHON implementation of the KINematic Molecular Simulation tool (*KinMS*¹⁵; T. A. Davis et al. 2013a), which was widely applied in the WISDOM (mm-Wave Interferometric Survey of Dark Object Masses) project (e.g., T. A. Davis et al. 2017; K. Onishi et al. 2017; I. Ruffa et al. 2023) and the Measuring Black Holes in Milky Way mass galaxies (MBHBM \star) project (D. D. Nguyen et al. 2020, 2022).

KinMS generates a mock data cube by simulating the gas distribution (Section 4.2) and kinematics while incorporating observational effects such as beam smearing, spatial and velocity binning, and LOS projection. The simulated cube is

¹⁰ <https://hla.stsci.edu/>

¹¹ <https://github.com/spacetelescope/tinytim/releases/tag/7.5>

¹² <https://www.stsci.edu/scientific-community/software/drizzlepac>

¹³ <https://www.astromatic.net/software/sextractor/>

¹⁴ https://www.stsci.edu/files/live/sites/www/files/home/hst/instrumentation/legacy/wfpc2/_documents/wfpc2_dhb.pdf

¹⁵ <https://github.com/TimothyADavis/KinMSpy>

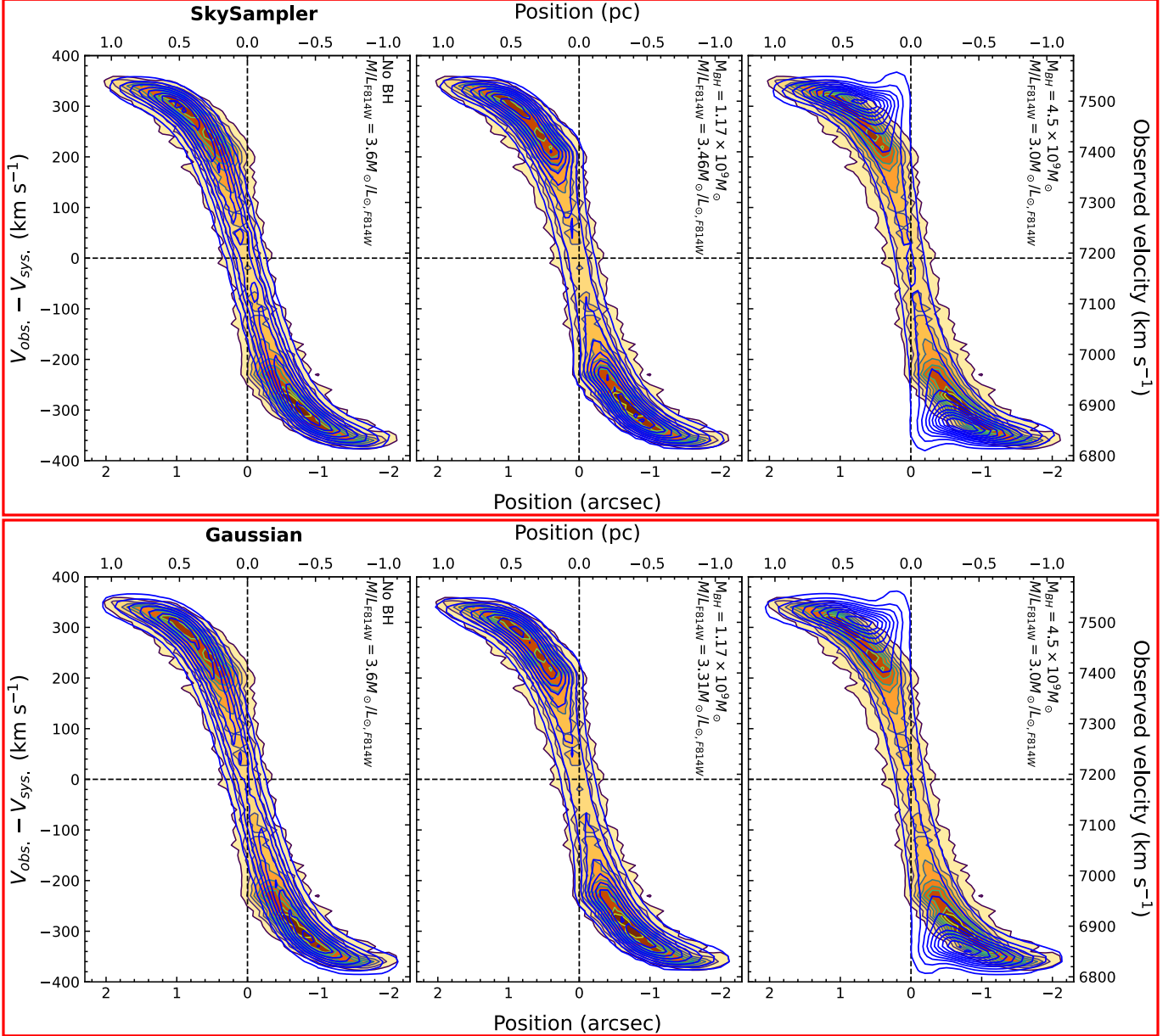


Figure 6. *Upper panels:* PVDs comparing the ALMA $^{12}\text{CO}(2-1)$ observations (orange-filled contours) with KinMS models (blue contours) constructed using the SKYSAMPLER gas distribution. The PVDs are extracted along the galaxy’s major axis at a position angle of $\Gamma = 175^\circ$ for three SMBH masses: no black hole (left), the best-fitting SMBH (middle), and an overmassive SMBH (right). The SMBH mass and M/L_{F814W} are indicated in the top-right of each panel. Black dashed lines mark the dynamical center, defined by the peak of the 1.3 mm continuum (Section 2.2), with the intersection corresponding to the systemic velocity ($v_{\text{sys}} = 7190 \text{ km s}^{-1}$) shown on the velocity axis. *Lower panels:* Same as above, but for KinMS models assuming a Gaussian gas surface brightness distribution.

compared directly with the observed cube to determine the best-fitting parameters and their uncertainties using a Markov chain Monte Carlo (MCMC) χ^2 minimization routine with Bayesian priors (Section 4.3). In constructing the KinMS model, we assumed the $^{12}\text{CO}(2-1)$ gas follows circular orbits around the galactic center under the combined gravitational potentials of the SMBH, stellar, and gas components. The circular velocity as a function of radius was computed using

the `mge_vcirc` routine from the Jeans Anisotropic Modeling framework (JAM¹⁶; M. Cappellari 2008).

Our adopted KinMS models fit the observed data by optimizing nine free parameters. The first two are the kinematic center coordinates (x_{cen} and y_{cen}), which specify the SMBH position relative to the data cube phase center or the con-

¹⁶ v7.2.4: <https://pypi.org/project/jampy/>

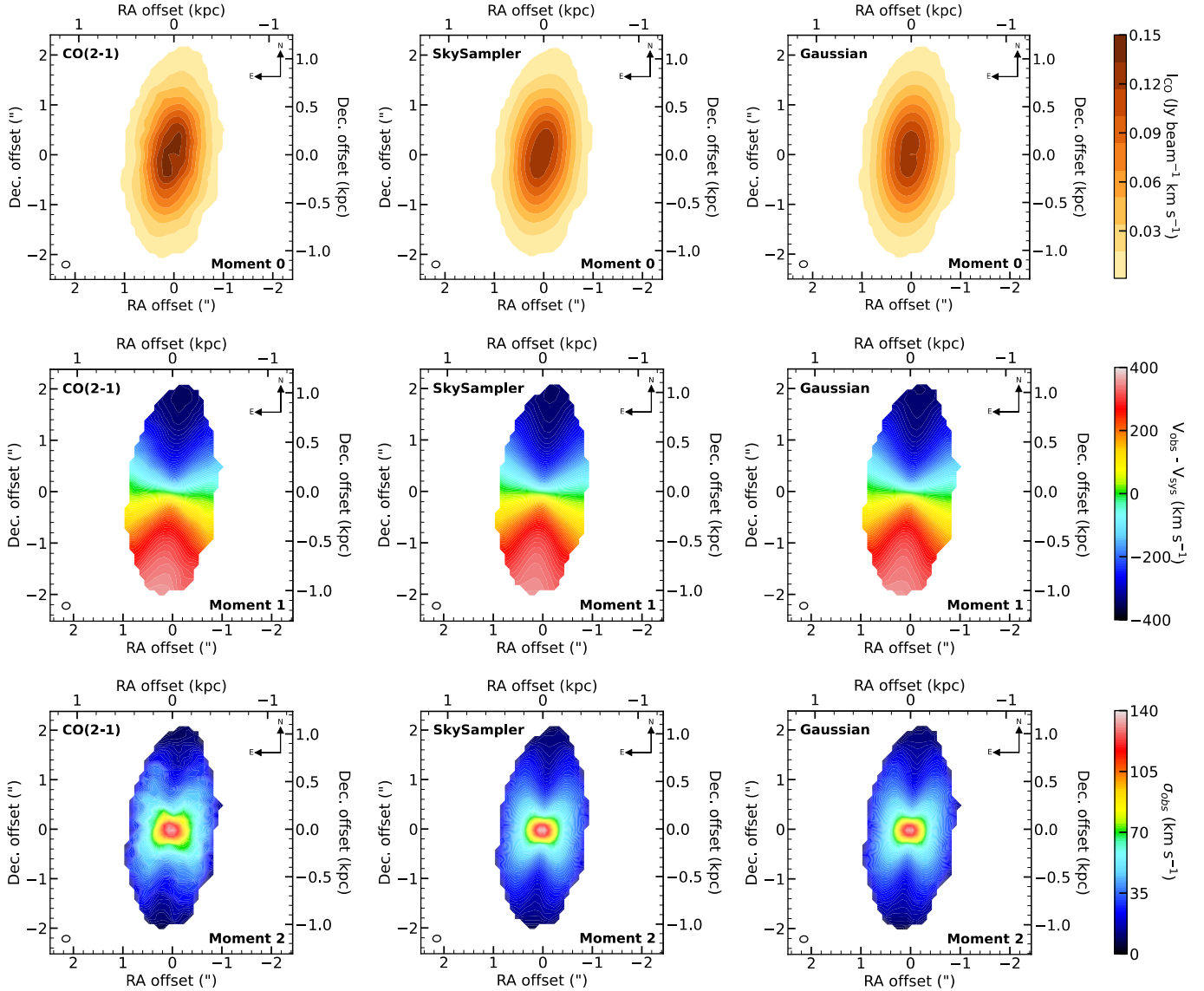


Figure 7. Comparison of the $^{12}\text{CO}(2-1)$ moment maps from our ALMA observations (left), the best-fitting KinMS model using the SKYSAMPLER tool to describe the gas distribution (middle), and the best-fitting KinMS model assuming a Gaussian gas distribution (right). All panels use identical color scales for direct comparison, demonstrating the strong consistency between the observed data and both models.

tinuum peak identified in Section 2.2. This assumption is justified, as any offset between the kinematic and photometric centers is typically much smaller than the synthesized beam. The third parameter is the systemic velocity of the gas disc (v_{sys}), or equivalently the velocity offset (v_{off}) if v_{sys} has already been subtracted. The fourth is the integrated intensity scaling factor (f , Section 4.2), describing the normalization of the gas distribution. The next three parameters characterize the CND morphology: inclination (i), position angle (Γ), and the intrinsic turbulent velocity dispersion of the gas (σ_{gas}). The final two parameters are the SMBH mass (M_{BH}) and the stellar mass-to-light ratio in the F814W band (M/L_{F814W}). These nine free parameters are summarized in Table 8.

4.2. Gas Distribution

Because our modeling fits the full 3D ALMA cube, a parameterized gas distribution is required and scaled by the integrated intensity factor (f) to match the observations. In this work, we represent the gas distribution using either the SKYSAMPLER¹⁷ CLEAN-component model derived directly from the data cube (Section 4.2.1) or an analytic axisymmetric profile (Section 4.2.2).

4.2.1. Gas Distribution Assumed by SKYSAMPLER

SKYSAMPLER constructs the molecular gas clouds in the $^{12}\text{CO}(2-1)$ CND of NGC 4061 directly from the CLEAN

¹⁷ <https://github.com/Mark-D-Smith/KinMS-skySampler>

Table 8. Best-fitting KINMS parameters and their uncertainties

Model parameters	Search range	Initial guesses	Best-fit values	1σ (16–84%)	3σ (0.14–99.86%)
(1)	(2)	(3)	(4)	(5)	(6)
SKYSAMPLER ($\chi^2_{\text{red,min}} \approx 0.80$)					
<u>Mass model:</u>					
$\lg(M_{\text{BH}}/\text{M}_{\odot})$	7 → 11	9	9.07	+0.03,–0.04	+0.10,–0.11
$M/L_{\text{F814W}} (\text{M}_{\odot}/\text{L}_{\odot})$	0 → 5	3.5	3.46	+0.07,–0.06	+0.20,–0.17
<u>$^{12}\text{CO}(2-1)$ CND:</u>					
$f (\text{Jy km s}^{-1})$	1 → 50	25	25.78	+0.71,–0.70	+2.06,–2.00
$i (\text{°})$	42 → 90	60	60.41	+1.03,–1.11	+2.80,–3.36
$\Gamma (\text{°})$	150 → 200	175	174.62	+0.50,–0.50	+1.44,–1.47
$\sigma_{\text{gas}} (\text{km s}^{-1})$	0 → 50	20	13.91	+1.98,–1.93	+5.71,–5.29
<u>Nuisance:</u>					
$x_c (\text{arcsec})$	–0.2 → +0.2	0	–0.03	+0.01,–0.01	+0.02,–0.02
$y_c (\text{arcsec})$	–0.2 → +0.2	0	0.02	+0.01,–0.01	+0.02,–0.03
$v_{\text{off}} (\text{km s}^{-1})$	–50 → +50	0	–10.24	+1.61,–1.63	+4.67,–4.77
Gaussian ($\chi^2_{\text{red,min}} \approx 0.78$)					
<u>Mass model:</u>					
$\lg(M_{\text{BH}}/\text{M}_{\odot})$	7 → 11	9	9.07	+0.04,–0.04	+0.10,–0.12
$M/L_{\text{F814W}} (\text{M}_{\odot}/\text{L}_{\odot})$	0 → 5	3.5	3.31	+0.06,–0.06	+0.18,–0.16
<u>$^{12}\text{CO}(2-1)$ CND:</u>					
$f (\text{Jy km s}^{-1})$	1 → 50	25	27.20	+0.84,–0.84	+2.56,–2.40
$i (\text{°})$	42 → 90	60	62.11	+0.90,–0.94	+2.60,–2.86
$\Gamma (\text{°})$	150 → 200	175	174.36	+0.51,–0.51	+1.47,–1.47
$\sigma_{\text{gas}} (\text{km s}^{-1})$	0 → 50	20	15.51	+2.03,–1.92	+6.18,–5.41

Notes: When modeling the gas distribution with a simple Gaussian profile in KINMS we fixed the nuisance parameters to their best-fit values obtained from the previous case that used the SKYSAMPLER tool to constrain the gas distribution.

components of the data cube, allowing the model to fit only the gas kinematics without assuming a specific spatial distribution. This approach introduces a single free parameter—the total flux scaling factor (f)—which rescales the cube to match the observed flux. Because CLEAN components omit residual emission from the deconvolution process, their total flux is slightly lower than that of the original cube; f compensates for this difference and ensures flux conservation within the modeled region.

We uniformly sampled the CLEAN components with 10^6 gas particles using the `sampleClouds` routine, reproducing the observed CO surface brightness distribution after beam convolution. The particles were then deprojected from the sky plane to the intrinsic galaxy plane with `transformClouds`, adopting a position angle of $\Gamma = 175^\circ$ and an inclination of $i = 60^\circ$.

Although Panel D of Figure 2 shows spatial variations in velocity dispersion, these are largely caused by beam smearing and projection effects in the highly inclined disc. We therefore adopted a constant σ_{gas} and modeled the gas as a geometrically thin disk with zero scale height in our KINMS simulations.

4.2.2. Gaussian Distribution

Given the smooth, centrally concentrated morphology of the $^{12}\text{CO}(2-1)$ CND (Section 2.5), we alternatively modeled it with a single Gaussian profile (e.g., D. D. Nguyen et al. 2020) without deprojection (fixed $q_j = 1$), as shown in Figure 5. This Gaussian profile is centered at an offset of $\mu = 0''.09$ (46.8 pc) with a dispersion of $\sigma = 0''.79$ (410.8 pc, corresponding to FWHM = $1''.87$ or 972.4 pc); these parameters are held fixed in the corresponding KINMS models. In this case, only the amplitude parameter (f) is allowed to vary, with the same interpretation as in Section 4.2.1.

4.3. Bayesian Inference and Priors

We employed the adaptive Metropolis algorithm (H. Haario et al. 2001), implemented within a Bayesian framework using the ADAMET¹⁸ package (M. Cappellari et al. 2013b), to constrain the best-fitting parameters of the KINMS model and estimate their statistical and formal uncertainties, which are propagated from the $^{12}\text{CO}(2-1)$ -CND kinematics measured

¹⁸ v2.0.9; <https://pypi.org/project/adamet/>

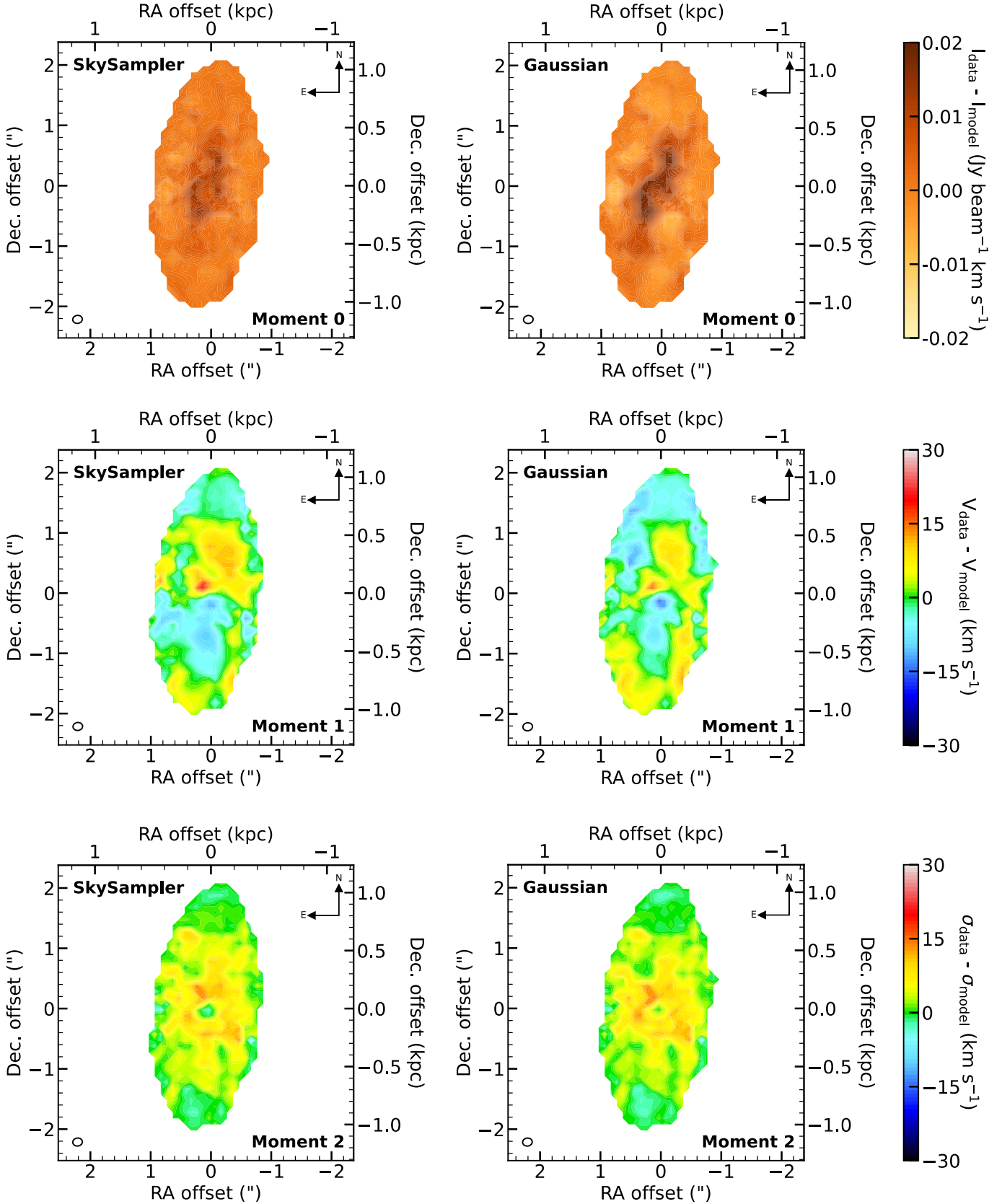


Figure 8. Moment-residual maps (data-model), obtained by subtracting the moment maps of the best-fitting KinMS models from the observations. The residuals are $\lesssim 10\%$ for the model using SKYSAMPLER and $\lesssim 13\%$ for the Gaussian model, demonstrating good agreement between the data and both models and indicating no significant non-circular motions or warps in the $^{12}\text{CO}(2-1)$ -CND of NGC 4061.

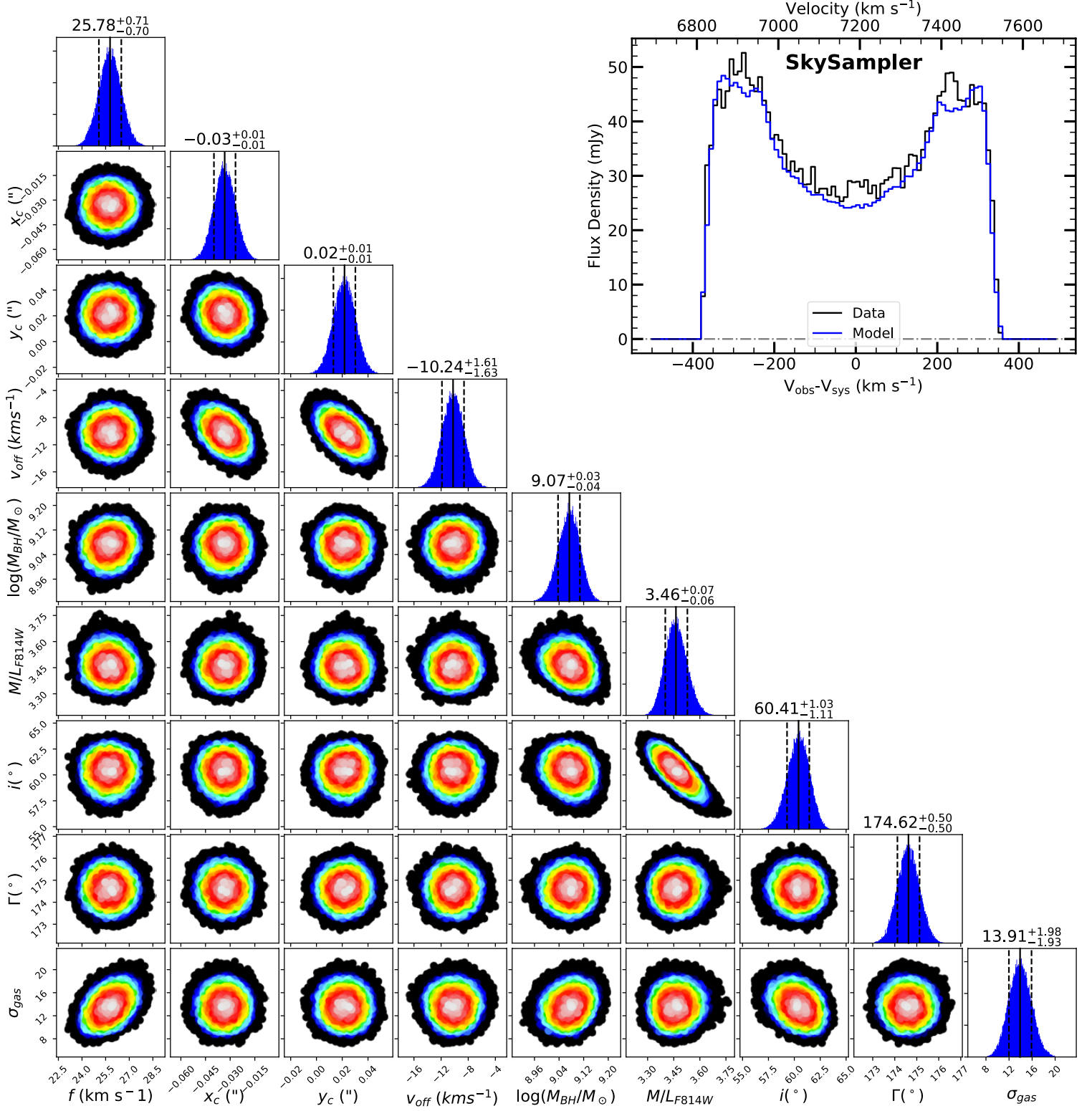


Figure 9. *Triangle:* Corner plot showing the posterior distributions from the KINMS model assuming the gas distribution derived with the SKYSAMPLER tool. The top panels display the 1D marginalized posterior distributions for each parameter, with vertical lines indicating the best-fit values and 1σ uncertainties (see text for details). The lower panels show 2D projections of parameter pairs, with colors indicating CLs: white, red, green, and black correspond to the best-fit 1σ , 2σ , 3σ , and larger than 3σ CLs, respectively. The numerical results are summarized in Table 8. *Insert panel:* Comparison of the ALMA $^{12}\text{CO}(2-1)$ integrated spectrum (panel E of Figure 2) with the same profile extracted from the best-fitting KINMS model, which highlights the good agreement between the data and model.

from our ALMA observations. Each MCMC chain consisted of 10^5 iterations, with the first 20% discarded as burn-in. The remaining samples were used to construct the posterior probability distribution functions (PDFs). Best-fit values were taken as the parameters corresponding to the maximum likelihood, and uncertainties were estimated at the 1σ (16–84%) and 3σ (0.14–99.86%) confidence levels (CLs). Because the search range of the M_{BH} parameter spans several orders of magnitude, it was sampled logarithmically, while all other parameters were sampled linearly. Convergence and adequate sampling of the parameter space were verified through inspection of the MCMC chains, using the parameter ranges and initial guesses summarized in Section 8.

In the Bayesian framework, the priors are proportional to the logarithm of the likelihood, $\ln(\text{data}|\text{model}) \propto 0.5\chi^2$, where χ^2 is defined as:

$$\chi^2 \equiv \sum_i \frac{(\text{data}_i - \text{model}_i)^2}{\sigma_i^2} = \frac{1}{\sigma_{\text{RMS}}^2} \sum_i (\text{data}_i - \text{model}_i)^2,$$

where σ_{RMS} is defined by the mask in Section 2.4 and were assumed as a constant σ for all pixels. When computing χ^2 , we rescaled the data cube uncertainties by a factor of $(2N)^{0.25} \approx 20$, where $N = 78,100$ is the number of pixels with detected emission. This scaling yields more realistic fit uncertainties by accounting for underestimated systematic effects commonly encountered in Bayesian analyses of large datasets such as ALMA (H. N. Ngo et al. 2025), VLT/MUSE (S. Thater et al. 2022, 2023), and JWST/NIRSpec (D. D. Nguyen et al. 2025c, 2026) observations. These effects arise from correlated noise between adjacent pixels, a result of the synthesized beam size inherent to interferometric data cube—an effect known as “noise covariance” (K. Onishi et al. 2017; E. V. North et al. 2019; D. D. Nguyen et al. 2020). This approach was first proposed by R. C. E. van den Bosch & G. van de Ven (2009), later refined by M. Mitzkus et al. (2017), and subsequently adopted in multiple WISDOM (e.g., E. V. North et al. 2019; M. D. Smith et al. 2019) and MBHBM★ (e.g., D. D. Nguyen 2019) studies.

4.4. Results

Given the synthesized beam size of our combined ALMA $^{12}\text{CO}(2-1)$ observations is approximately equal to the expected SOI of the tentative SMBH, the comparison between the observed molecular gas kinematics and our KinMS models reveals clear evidence for a central SMBH, as indicated by a modest rise in rotation velocity toward the nucleus at radii smaller than $0.^{\prime}4$ (see Figure 6). As summarized in Table 8, the best-fitting KinMS model using the SKYSAMPLER tool yields $M_{\text{BH}} = (1.17^{+0.08}_{-0.10}) \times 10^9 M_{\odot}$ and $M/L_{\text{F814W}} = 3.46^{+0.07}_{-0.06} (M_{\odot}/L_{\odot})$. A comparable model employing a Gaussian disk provides $M_{\text{BH}} = (1.17^{+0.11}_{-0.10}) \times 10^9 M_{\odot}$ and $M/L_{\text{F814W}} = 3.31 \pm 0.06 (M_{\odot}/L_{\odot})$. The SKYSAMPLER

model achieves a minimum $\chi^2_{\text{min}} = 62,472$, corresponding to a reduced $\chi^2_{\text{red,min}} = 0.80$, while the Gaussian model yields $\chi^2_{\text{min}} = 60,913$ and $\chi^2_{\text{red,min}} = 0.78$. All quoted uncertainties represent 1σ confidence intervals (CLs) unless otherwise stated; both 1σ and 3σ CLs are reported in Table 8 and Table 9.

Both best-fitting models reproduce the ALMA $^{12}\text{CO}(2-1)$ data remarkably well across all spatial positions of the CND. This agreement is evident in the middle panels of Figure 6 and in Figure 7, which compare the observed and modeled PVDs) along the major axis and the corresponding moment maps directly and respectively.

In each modeling approach, whether using SKYSAMPLER or a Gaussian surface brightness distribution, Figure 6 also includes two comparative KinMS models. The first assumes no SMBH ($M_{\text{BH}} = 0 M_{\odot}$) with $M/L_{\text{F814W}} = 3.6 (M_{\odot}/L_{\odot})$, which reproduces the extended CND kinematics beyond $r > 0.^{\prime}4$ but fails to match the slightly central rise in rotation velocity ($\approx 80 \text{ km s}^{-1}$). This no-SMBH model also modestly overpredicts ($\approx 35 \text{ km s}^{-1}$) the CDN’s rotation at radii beyond $1.^{\prime\prime}$. The second adopts a larger fixed SMBH mass of $M_{\text{BH}} = 4.5 \times 10^9 M_{\odot}$ with $M/L_{\text{F814W}} = 3.0 (M_{\odot}/L_{\odot})$; it similarly fits the outer kinematics but overpredicts the central velocity increase at small radii. In all these alternative models, only M/L_{F814W} was allowed to vary, while M_{BH} was held fixed at the specified values and all other parameters were kept at their best-fit values listed in Table 8.

Figure 8 further evaluates the consistency between our ALMA observations and the best-fitting KinMS models by examining the residual maps of all three moments to assess which model provides the better representation visually. The residuals show no discernible structures in either the integrated intensity (top panels) or the intensity-weighted mean LOS velocity dispersion maps (bottom panels). Any signatures of non-circular motions (e.g., inflows or outflows) within the $^{12}\text{CO}(2-1)$ CND are negligible, as indicated by the intensity-weighted mean LOS velocity residuals ($V_{\text{residual}} = V_{\text{data}} - V_{\text{model}}$; middle panels). The best-fitting KinMS model using the SKYSAMPLER tool yields residual velocities of $|V_{\text{residual}}| \lesssim 15 \text{ km s}^{-1}$ ($\lesssim 4\%$) across the CND, comparable to the spectral channel width of the reduced ALMA cube ($\approx 10 \text{ km s}^{-1}$), implying an absence of significant non-circular motions. The Gaussian-based model produces slightly smaller residuals of $|V_{\text{residual}}| \lesssim 10 \text{ km s}^{-1}$ ($\lesssim 3\%$), likely due to its assumption of a smooth gas distribution, which only approximates the observed morphology. In contrast, the SKYSAMPLER-based model incorporates the actual spatial gas distribution from the data cube, substantially reducing discrepancies in the intensity-weighted mean LOS velocity field. In this work, we adopt the average of both the SKYSAMPLER-based and the Gaussian-based best-fitting model as our fiducial result.

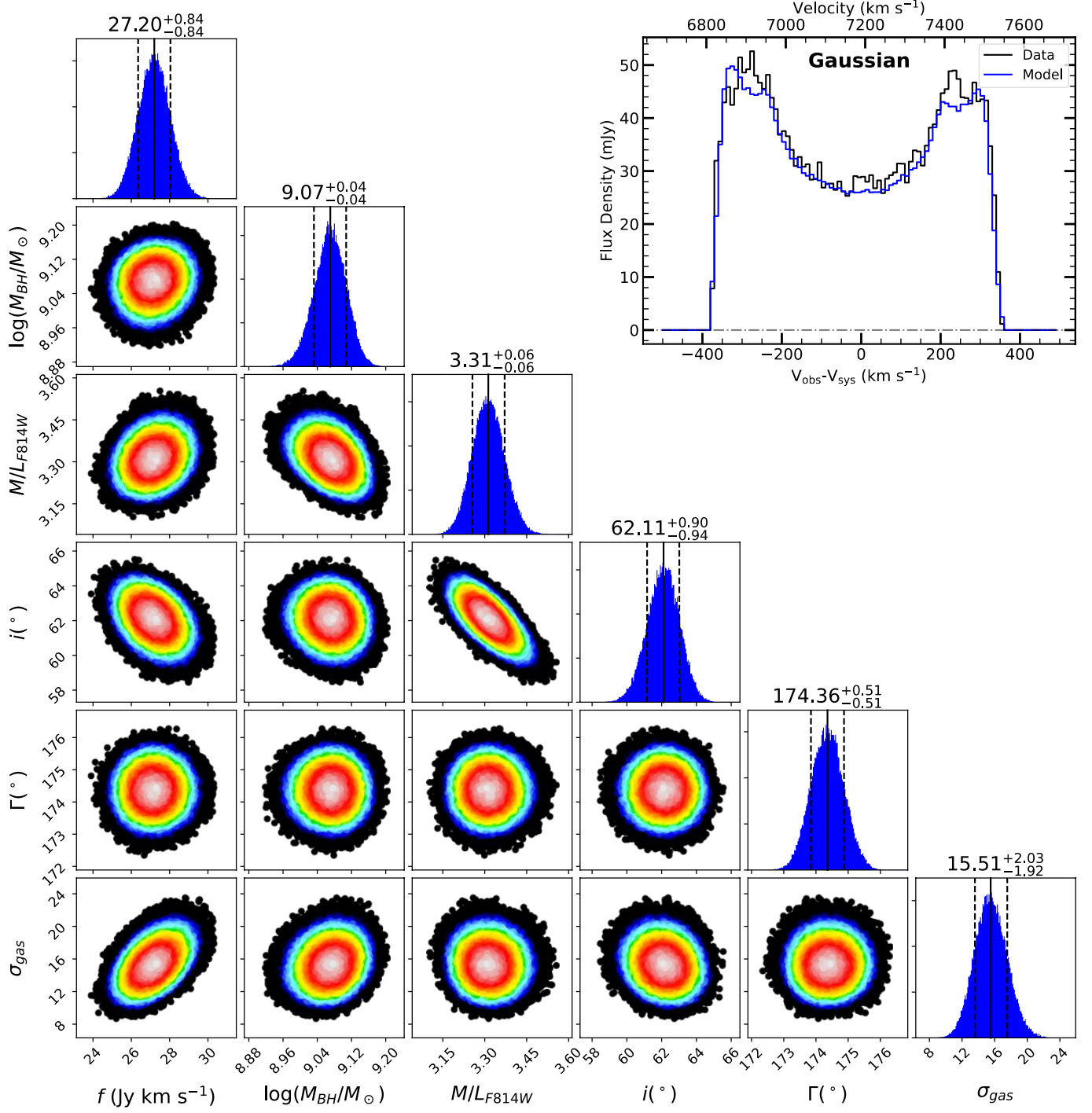


Figure 10. Same as Figure 9 but the KINMS model was assumed to be a Gaussian for gas surface brightness distribution.

Figure 9 (for the SKYSAMPLER-based KINMS models) and Figure 10 (for the Gaussian-based KINMS models) display the 2D posterior distributions for each pair of free parameters, marginalizing over the others, with colors indicating likelihood levels. White corresponds to the maximum likelihood within the 1σ CL, while blue denotes the 3σ CL. The 1D histograms along the diagonal show the marginalized distributions for each parameter, where the thick black vertical

lines indicate the best-fit values and the dashed lines mark their 1σ uncertainties. All distributions exhibit Gaussian-like shapes, demonstrating that the MCMC optimization of our KINMS models achieved robust convergence.

In both figures, we further assess the consistency between the observed $^{12}\text{CO}(2-1)$ emission and the best-fitting KINMS models by comparing their integrated spectra in the inset panels. The best-fit models not only reproduce the overall

kinematic structure but also recover the symmetric double-horn profile of the total integrated $^{12}\text{CO}(2-1)$ spectrum across the CND. These results confirm that the best-fitting models provide an accurate representation of the observed molecular gas kinematics.

We also verified the absence of significant non-circular motions or kinematic warps (i.e., variations in position angle, Γ , that would twist the isovelocity contours along the CND minor axis). Such effects could bias the dynamical modeling and M_{BH} estimation. As shown in Figure 11, the minor-axis PVD of NGC 4061, extracted along $\Gamma \approx 175^\circ + 90^\circ$, exhibits symmetry across all four “forbidden quadrants,” a feature also well reproduced by the best-fitting SKYSAMPLER-based KinMS model, confirming the overall regular rotation of the $^{12}\text{CO}(2-1)$ CND.

While the other model parameters are well constrained, a clear anti-correlation between M_{BH} and M/L_{F814W} is evident (see both Figure 9 and Figure 10). This degeneracy is commonly observed in spatially resolved dynamical modeling and arises because both stars and BH gravitational potentials affect the central circular motions of the $^{12}\text{CO}(2-1)$ CND.

Given that the angular resolution of our combined ALMA data matches the SMBH sphere of influence (SOI; the region surrounding a BH within which its gravitational influence dominates that of the surrounding stellar mass; equivalently, the radius (r_{soi}) where the enclosed stellar mass equals M_{BH}). It can also be calculated through the stellar velocity dispersion (σ) as $r_{\text{soi}} = GM_{\text{BH}}/\sigma^2$), implying that the SMBH SOI is resolved and explaining the observed $M_{\text{BH}}-M/L_{\text{F814W}}$ anti-correlation in the posterior distributions.

Additional covariances are also present among other parameters:

y_{cen} and v_{off} : resulting from the large beam size when the kinematic center is tied to the peak of the spatially resolved continuum emission (Section 2.2). Higher angular resolution observation will tighter constrain the CND disk center and suppress this degeneracy.

i and M/L_{F814W} : which emerges as the CND transitions from more edge-on to more face-on geometries (M. D. Smith et al. 2019); the moderate inclination of the $^{12}\text{CO}(2-1)$ CND in NGC 4061 ($i \approx 59^\circ$) reflects this behavior.

f and σ_{gas} : since f tends to normalize to the adopted surface brightness distribution (M. D. Smith et al. 2019; D. D. Nguyen et al. 2020).

Such parameter covariances are typical in simultaneous dynamical modeling of molecular gas disks.

Figure 12 presents the enclosed mass profiles of the SMBH, stellar component, and molecular gas within $2''$ of the $^{12}\text{CO}(2-1)$ CND. Although the molecular gas contributes

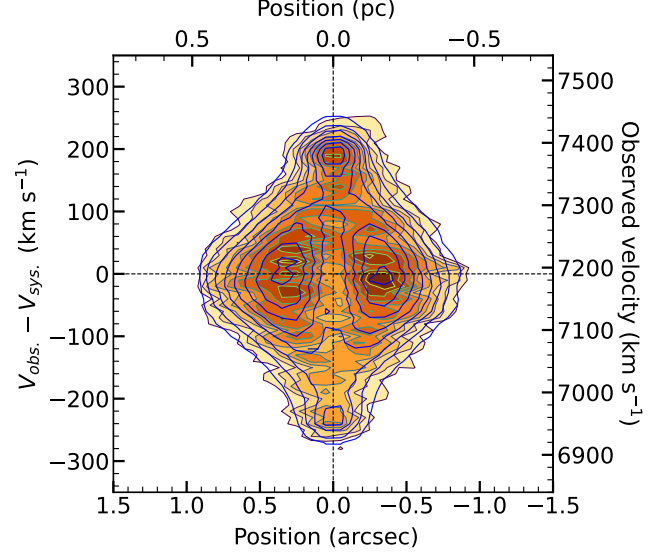


Figure 11. PVD extracted along the minor axis of the $^{12}\text{CO}(2-1)$ CND, oriented at a position angle of $\Gamma = 175^\circ + 90^\circ$, with a systemic velocity of $v_{\text{sys}} = 7190 \text{ km s}^{-1}$. The best-fitting SKYSAMPLER-based (blue) KinMS model is overplotted at the same contour levels.

nearly two orders of magnitude less mass than the stars over this region, the black hole dominates the gravitational potential inside $r \lesssim 0''.2$. Moreover, the synthesized beam of the combined ALMA data cube ($\theta_{\text{beam}} \approx 0''.13$) closely matches the estimated SOI radius of the SMBH ($r_{\text{soi}} \approx 0''.12$), calculated using our best-fit black hole mass and an assumed stellar velocity dispersion of $\sigma \approx 290 \text{ km s}^{-1}$ (J. C. Pinkney & Nuker Team 2005). This close correspondence between the observational angular resolution and the SMBH SOI provides strong support for the reliability of our M_{BH} measurement in NGC 4061.

4.5. Uncertainties

Several additional sources of uncertainty are inherent to dynamical modeling, including (i) the adopted distance to NGC 4061, (ii) the assumption of a thick disk (implemented via the z -coordinate perpendicular to the disk plane), (iii) the turbulent velocity dispersion of the gas, (iv) the disk inclination, (v) possible radial variations in the mass-to-light ratio, (vi) the construction of the stellar mass model without dust masking, and (vii) the use of an alternative photometric band. We discuss each of these effects in the following subsections.

4.5.1. Distances

Since the inferred M_{BH} scales linearly with the assumed distance ($M_{\text{BH}} \propto D$), the wide range of distance estimates for NGC 4061 (68–112 Mpc; NED)—primarily based on optical and near-infrared light curves of the Type Ia supernova SN 2008bf—constitutes the dominant source of uncertainty in our M_{BH} measurement. We adopt a distance of 107.2 Mpc

Table 9. Best-fitting M/L models' parameters and their uncertainties

Model	Search	Best-fit	1σ	3σ
parameters	range	values	(16–84%)	(0.14–99.86%)
(1)	(2)	(3)	(4)	(5)
SKYSAMPLER				
Linear M/L_{F814W} :		$\chi^2_{\text{red,min}} \approx 0.75$		
$\lg(M_{\text{BH}}/M_{\odot})$	7→11	9.11	±0.03	±0.10
M/L_0 (M_{\odot}/L_{\odot})	0→5	3.31	±0.05	±0.14
α (M_{\odot}/L_{\odot} per arcsec)	0→1	0.11	±0.02	±0.05
Gaussian M/L_{F814W} :		$\chi^2_{\text{red,min}} \approx 0.75$		
$\lg(M_{\text{BH}}/M_{\odot})$	7→11	9.10	±0.07	±0.20
M/L_0 (M_{\odot}/L_{\odot})	0→5	0.40	±0.24	±0.73
M/L_1 (M_{\odot}/L_{\odot})	0→5	3.13	±0.16	±0.49
σ_{Gaussian} (arcsec)	0→1	0.93	±0.33	±0.98
F555W MGE:		$\chi^2_{\text{red,min}} \approx 0.72$		
$\lg(M_{\text{BH}}/M_{\odot})$	7→11	9.15	±0.05	±0.15
M/L_{F555W} (M_{\odot}/L_{\odot})	0→10	7.02	±0.11	±0.34
Gaussian				
Linear M/L_{F814W} :		$\chi^2_{\text{red,min}} \approx 0.73$		
$\lg(M_{\text{BH}}/M_{\odot})$	7→11	9.14	±0.04	±0.13
M/L_0 (M_{\odot}/L_{\odot})	0→5	2.88	±0.11	±0.33
α (M_{\odot}/L_{\odot} per arcsec)	0→1	0.49	±0.10	±0.30
Gaussian M/L_{F814W} :		$\chi^2_{\text{red,min}} \approx 0.73$		
$\lg(M_{\text{BH}}/M_{\odot})$	7→11	9.09	±0.06	±0.17
M/L_0 (M_{\odot}/L_{\odot})	0→5	0.04	±0.09	±0.20
M/L_1 (M_{\odot}/L_{\odot})	0→5	3.32	±0.10	±0.28
σ_{Gaussian} (arcsec)	0→1	2.06	±0.28	±0.87
F555W MGE:		$\chi^2_{\text{red,min}} \approx 0.72$		
$\lg(M_{\text{BH}}/M_{\odot})$	7→11	9.13	±0.04	±0.11
M/L_{F555W} (M_{\odot}/L_{\odot})	0→10	6.94	±0.12	±0.29

Notes: In these KinMS models, we fixed all molecular gas and nuisance parameters at their best-fit values as of their default models listed in Section 8.

from the MASSIVE survey, derived from the galaxy's redshift (C.-P. Ma et al. 2014). The spread in published distances introduces a systematic uncertainty of $\approx 37\%$ in M_{BH} .

4.5.2. Thick Disk Assumption

In our KinMS modeling, we assumed a geometrically thin $^{12}\text{CO}(2-1)$ CND by fixing its vertical scale height to zero ($d = 0''$). Physically, the molecular disk may have a finite vertical extent, so we tested the impact of this assumption by introducing a constant vertical thickness as an additional free parameter. We performed this test using two independent surface-brightness prescriptions: one based on the SKYSAMPLER tool and another using a Gaussian profile. In both cases, the best-fit parameters were consistent with those in Table 8, differing by less than 5%. The inferred vertical thicknesses were $d = 0''.017 \pm 0''.003$ for the SKYSAMPLER model and $d = 0''.025 \pm 0''.005$ for the Gaussian model. Since both values are smaller than the synthesized beam, the assumption of a razor-thin $^{12}\text{CO}(2-1)$ disk is well justified for NGC 4061.

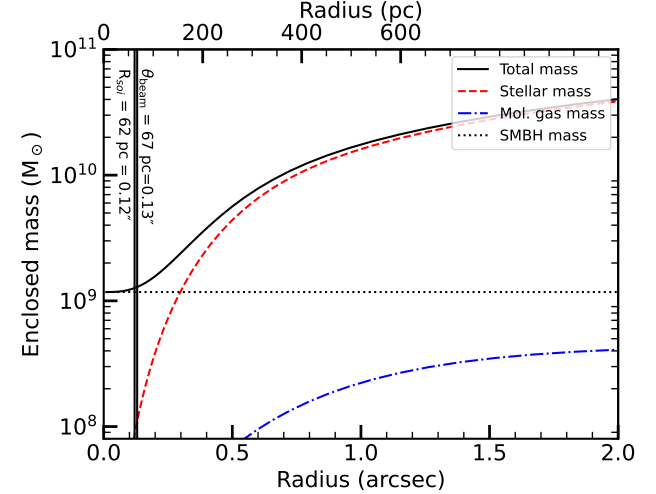


Figure 12. Enclosed mass of NGC 4061 (black solid line) as a function of radius, showing the contributions of all mass components: M_{BH} , stars, and ISM.

4.5.3. Turbulent Velocity Dispersion of the Gas

Although our KinMS models assumed a constant turbulent velocity dispersion for the $^{12}\text{CO}(2-1)$ CND, σ_{gas} may vary with both radius and azimuth across the disk. Moreover, beam smearing can artificially increase the central velocity dispersion, potentially overestimate the inferred M_{BH} . To evaluate these effects on the M_{BH} uncertainty, we parameterized σ_{gas} to several functional forms below. Here, we imposed a lower limit of $\sigma_{\text{gas,min}} = 1 \text{ km s}^{-1}$ to prevent unrealistically narrow line profiles (A. J. Barth et al. 2016):

Linearity: $\sigma_{\text{gas}}(r) = \alpha \times r + \beta$, where α and β are free parameters. The fits yielded $\alpha \approx 0$, with $\beta = 13.91 \text{ km s}^{-1}$ for the SKYSAMPLER model and $\beta = 15.51 \text{ km s}^{-1}$ for the Gaussian model. All other best-fitting KinMS parameters remain consistent with those from the constant-dispersion models presented in Section 4.4 and Table 8.

Exponential: $\sigma_{\text{gas}}(r) = \sigma_0 \exp(-r/r_0) + \sigma_1$, where σ_0 , σ_1 , and r_0 are free parameters. The best-fitting KinMS model using the SKYSAMPLER tool yields $M_{\text{BH}} = (1.23^{+0.22}_{-0.18}) \times 10^9 M_{\odot}$ and $M/L_{\text{F814W}} = 3.44 \pm 0.08 (M_{\odot}/L_{\odot})$, with $\sigma_0 = 83.45 \pm 3.27 \text{ km s}^{-1}$, $\sigma_1 = 14.15 \pm 0.55 \text{ km s}^{-1}$, and $r_0 = 0''.09 \pm 0''.04$. The corresponding model assuming a Gaussian gives $M_{\text{BH}} = (1.20^{+0.21}_{-0.18}) \times 10^9 M_{\odot}$ and $M/L_{\text{F814W}} = 3.37 \pm 0.07 (M_{\odot}/L_{\odot})$, with $\sigma_0 = 65.98 \pm 1.14 \text{ km s}^{-1}$, $\sigma_1 = 13.03 \pm 0.29 \text{ km s}^{-1}$, and $r_0 = 0''.12 \pm 0''.04$.

Gaussian: $\sigma_{\text{gas}}(r) = \sigma_0 \exp[-(r - r_0)^2/2\mu^2] + \sigma_1$, where σ_0 , σ_1 , μ , and r_0 are free parameters. The parameter r_0 was allowed to vary over positive and negative values to account for potential offsets of the velocity-dispersion peak from the center. The best-fitting KinMS model using the SKYSAMPLER tool yields $M_{\text{BH}} = (1.20^{+0.18}_{-0.16}) \times 10^9 M_{\odot}$ and $M/L_{\text{F814W}} = 3.47 \pm 0.06 (M_{\odot}/L_{\odot})$, with $\sigma_0 = 69.63 \pm 2.87 \text{ km s}^{-1}$, $\sigma_1 =$

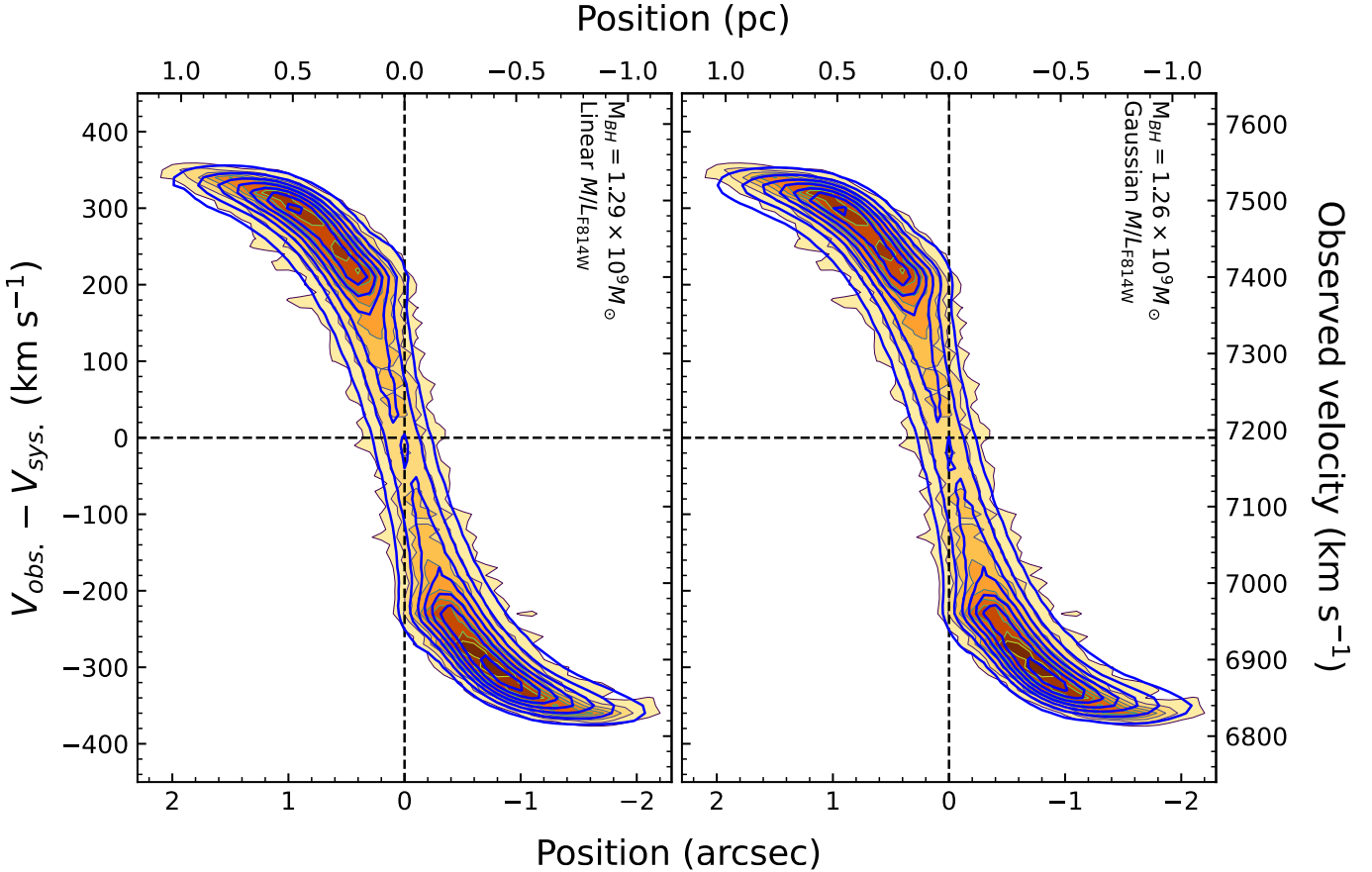


Figure 13. Position–velocity diagrams along the major axis for the best-fitting KINMS models, in which the $^{12}\text{CO}(2-1)$ gas surface-brightness distribution is described using the SKYSAMPLER tool. Models adopting linear (left) and Gaussian (right) $M/L_{\text{F814W}}(r)$ profiles are shown.

$9.87 \pm 0.38 \text{ km s}^{-1}$, $r_0 = 0''.01 \pm 0''.001$, and $\mu = 0''.01 \pm 0''.001$. The corresponding model assuming a Gaussian gas distribution gives $M_{\text{BH}} = (1.23^{+0.15}_{-0.13}) \times 10^9 M_{\odot}$ and $M/L_{\text{F814W}} = 3.37 \pm 0.07 (M_{\odot}/L_{\odot})$, with $\sigma_0 = 71.04 \pm 1.22 \text{ km s}^{-1}$, $\sigma_1 = 13.49 \pm 1.35 \text{ km s}^{-1}$, $r_0 = 0''.01 \pm 0''.001$, and $\mu = 0''.01 \pm 0''.001$.

These results indicate that assuming a constant σ_{gas} provides an adequate description of the $^{12}\text{CO}(2-1)$ disk kinematics for M_{BH} dynamical modeling. While the choice of radial parameterization for $\sigma_{\text{gas}}(r)$ does influence the inferred M_{BH} , the effect is modest: adopting a linear gradient yields negligible changes, and the resulting systematic uncertainties are $\lesssim 5\%$ and $\lesssim 5\%$ for the exponential and Gaussian $\sigma_{\text{gas}}(r)$ profiles, respectively.

4.5.4. Inclination

In nearly face-on CNDs (inclination $\lesssim 30^\circ$), dynamical models often struggle to constrain both the SMBH mass and stellar M/L , leading to large uncertainties and asymmetric posterior distributions (e.g., M. D. Smith et al. 2019). This limitation arises because the deprojection of the MGE into a 3D intrinsic stellar mass model becomes degenerate when the system is viewed close to face-on. In contrast, NGC 4061

exhibits a well-constrained $^{12}\text{CO}(2-1)$ -CND inclination of $i \approx 60^\circ$, allowing for a unique 3D deprojection of the stellar mass distribution. Consequently, inclination-related uncertainties in our derived M_{BH} and M/L_{F814W} are negligible (see Figure 9 and Figure 10).

4.5.5. Mass-to-Light Ratio Model Variations

Our fiducial analysis adopts a spatially constant M/L_{F814W} . In reality, however, M/L_{F814W} may exhibit radial variations as a result of mass segregation (D. D. Nguyen et al. 2025a), potentially giving rise to a centrally enhanced profile that could partially mimic, or augment, the dynamical signature of a compact central dark mass. To investigate this effect, we constructed a set of test models using the same framework described in Section 4.3, but allowing for radially varying M/L_{F814W} profiles. Specifically, we considered two functional forms: (1) a linear profile, $M/L_{\text{F814W}}(r) = M/L_0 + \alpha \times r$, and (2) a Gaussian profile, $M/L_{\text{F814W}}(r) = M/L_0 \exp(-r^2/2\sigma_{\text{Gaussian}}^2) + M/L_1$, where M/L_0 denotes the central mass-to-light ratio in both cases, α is the linear gradient, M/L_1 is a constant offset, and σ_{Gaussian} characterizes the Gaussian width. For these experiments, all nuisance parameters and molecular gas properties were

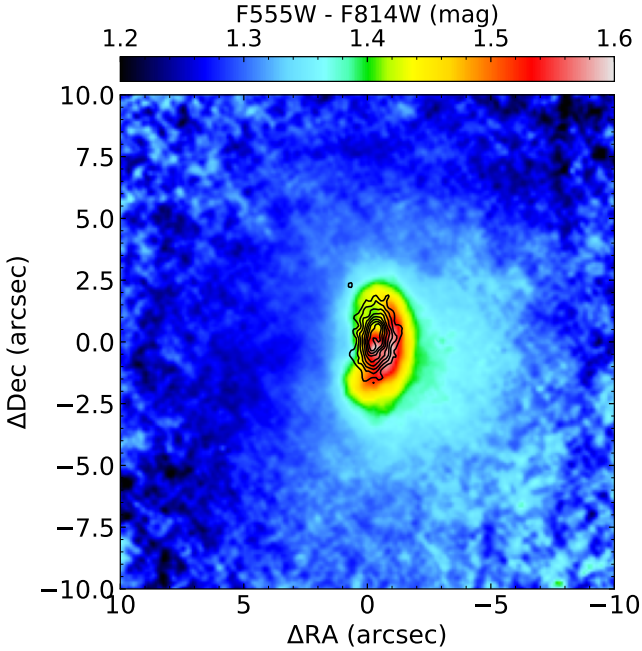


Figure 14. The $^{12}\text{CO}(2-1)$ contours are overlaid on the nuclear F555W–F814W color map of NGC 4061 derived from *HST*/WFPC2 images, showing their spatial coincidence with the prominent dust lane. The observed color variations are clearly dominated by dust extinction rather than changes in the underlying stellar population.

held fixed at their best-fitting values from the fiducial models (Table 8). At the same time, the M_{BH} was allowed to vary freely. The resulting KinMS models were analyzed within the same Bayesian framework, and the corresponding best-fit parameters are summarized in Table 9.

Figure 13 compares the two preferred KinMS models that adopt the SKYSAMPLER prescription for the $^{12}\text{CO}(2-1)$ surface brightness distribution, for each of the radially varying $M/L_{\text{F814W}}(r)$ parameterizations. Both the linear and Gaussian $M/L_{\text{F814W}}(r)$ profiles reproduce the observed $^{12}\text{CO}(2-1)$ kinematics across the circumnuclear disk, despite the absence of independent observational evidence for color gradients or stellar population variations in the central region of NGC 4061. Relative to the fiducial models assuming a constant M/L_{F814W} (Section 4.4; Table 8), the inferred M_{BH} values differ by less than 10% for the linear profile and less than 7% for the Gaussian profile, remaining fully consistent within the quoted 1σ uncertainties. Consistent results are also obtained for KinMS models that assume a Gaussian functional form for the $^{12}\text{CO}(2-1)$ surface brightness, for which the inferred M_{BH} values differ by less than 17% for the linear profile and less than 5% for the Gaussian profile, and likewise agree within the 1σ uncertainties.

To further investigate the issue of possible spatial M/L_{F814W} variation, we constructed a F555W–F814W color map using an additional *HST*/F555W image in combination

with the F814W image (Figure 14). Before generating the color map, the astrometrically aligned images were cross-convolved with each other’s PSFs (i.e., the F555W image convolved with the F814W PSF and vice versa) to minimize artificial color gradients arising from differences in PSF width. We then subtracted the sky background from each image, measured within an annulus spanning $(35-40)''$ from the galaxy center. The resulting color map reveals a spatial coincidence between the $^{12}\text{CO}(2-1)$ contours and regions of enhanced F555W–F814W color, while the remainder of the nuclear region exhibits nearly uniform color. This correspondence indicates that the observed color variations are dominated by dust extinction rather than intrinsic changes in the stellar population.

These findings demonstrate that our ALMA-based measurement of M_{BH} is only weakly sensitive to the assumed stellar mass-to-light ratio profile, including plausible variations driven by dust attenuation or stellar population changes across the $^{12}\text{CO}(2-1)$ CND. This insensitivity reflects the dominance of the central black hole over the gravitational potential within the inner $0''.2$. We therefore conclude that uncertainties associated with the stellar mass model contribute at the $\sim 10\%$ level to the total error budget of M_{BH} .

4.5.6. F814W MGE Stellar Mass Model without Dust Masking

In constructing the fiducial *HST*/WFPC2 F814W MGE stellar mass model, we masked the prominent central dust lane visible in the *HST* image. However, the total molecular gas mass inferred from the $^{12}\text{CO}(2-1)$ circumnuclear disk (extending to $r \lesssim 2''$) is nearly two orders of magnitude smaller than the enclosed stellar mass within the same radius (Figure 12). To assess the potential impact of dust obscuration on our SMBH mass measurement, we repeated the MGE modeling without applying a dust mask. The resulting dust-unmasked *HST*/WFPC2 F814W MGE model was then adopted as the stellar mass input for both sets of KinMS models. Using the SKYSAMPLER prescription for the CND surface brightness, we obtained $M_{\text{BH}} = (7.41 \pm 1.92) \times 10^8 \text{ M}_{\odot}$ and $M/L_{\text{F814W}} = 5.50 \pm 0.16 (\text{M}_{\odot}/\text{L}_{\odot})$. The corresponding model employing a simple Gaussian surface brightness profile yields $M_{\text{BH}} = (6.92 \pm 1.16) \times 10^8 \text{ M}_{\odot}$ and $M/L_{\text{F814W}} = 5.42 \pm 0.06 (\text{M}_{\odot}/\text{L}_{\odot})$. The close agreement between these results and those from the dust-masked models demonstrates that dust attenuation has a negligible impact on our dynamical determination of M_{BH} .

4.5.7. Using the Alternative F555W MGE Stellar Mass Model

We assessed the effect of adopting an alternative stellar mass model derived from the *HST*/WFPC2 F555W image on our dynamical determination of M_{BH} . In this test, we replaced the fiducial *HST*/WFPC2 F814W MGE model described in Section 3 with the corresponding F555W-based MGE model. For consistency, we adopted a photometric

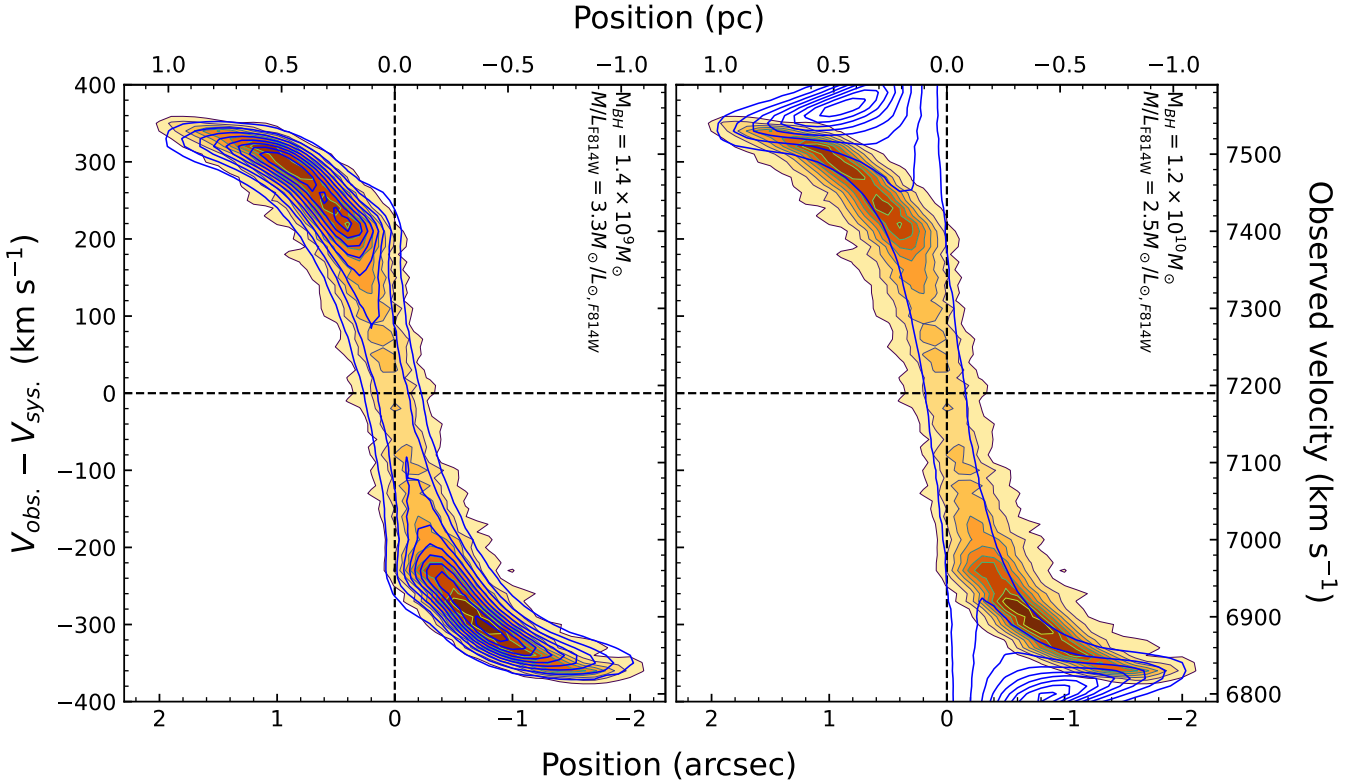


Figure 15. Position–velocity diagrams along the major axis for the SKYSAMPLER-based KinMS models are shown for two assumed SMBH masses calibrated following the J. Kormendy & L. C. Ho (2013) $M_{\text{BH}}-\sigma$ correlations and a constant M/L_{F814W} . The left panel adopts $M_{\text{BH}} = 2.0 \times 10^9 M_{\odot}$, inferred from the central stellar velocity dispersion of $\sigma \approx 290 \text{ km s}^{-1}$ measured by J. C. Pinkney & Nuker Team (2005). The right panel adopts a substantially larger mass, $M_{\text{BH}} = 1.2 \times 10^{10} M_{\odot}$, corresponding to the high stellar velocity dispersion of $\sigma \approx 459 \text{ km s}^{-1}$ listed in the Hypercat catalog. Both models fail to describe the $^{12}\text{CO}(2-1)$ -CND’s central rotation.

zero point of 24.683 mag and a solar absolute magnitude of 4.82 mag (C. N. A. Willmer 2018) in the F555W band. This alternative stellar mass model was then implemented within the KinMS framework, considering both the SKYSAMPLER and Gaussian prescriptions for the $^{12}\text{CO}(2-1)$ CND’s surface brightness. In these tests, only M_{BH} and the stellar M/L_{F555W} were treated as free parameters, while all remaining model parameters were fixed to their best-fitting values from the fiducial models (Table 8). The resulting best-fit values of M_{BH} and M/L_{F555W} for both modeling approaches are summarized in Table 9. Overall, adopting the F555W-based stellar mass model introduces an additional uncertainty of approximately 20% in the inferred SMBH mass for NGC 4061, likely reflecting the greater sensitivity of the F555W band to dust attenuation compared to the F814W band.

4.6. The Reliability of Our Measurements

Following the argument of S. P. Rusli et al. (2013a), the impact of observational angular resolution on the precision of M_{BH} measurements can be quantified by the resolving power $\zeta = 2r_{\text{soi}}/\theta_{\text{FWHM}}$, where r_{soi} is the SMBH SOI radius and θ_{FWHM} is the synthesized beam size. Observations with $\zeta \geq 2$ (i.e., $\theta_{\text{FWHM}} \leq r_{\text{soi}}$) are generally sufficient to yield

precise M_{BH} determinations (e.g., E. V. North et al. 2019; B. D. Boizelle et al. 2021). For $\zeta < 2$, the inferred M_{BH} values remain useful (e.g., T. A. Davis 2014; D. D. Nguyen et al. 2020), but typically exhibit larger uncertainties and increased sensitivity to systematics, including uncertainties in the stellar mass profile and beam-smearing effects (S. P. Rusli et al. 2013b; A. J. Barth et al. 2016; D. D. Nguyen et al. 2021). In the case of NGC 4061, our ALMA data correspond to $\zeta \approx 2$, indicating that the dynamical- M_{BH} measurement presented in this work is robust.

As discussed in Section 1, previous estimates of the SMBH mass in NGC 4061 relied solely on the $M_{\text{BH}}-\sigma$ relation (e.g., J. Kormendy & L. C. Ho 2013), using low-spatial-resolution measurements of the velocity dispersion of either the stellar ($\sigma \approx 290 \text{ km s}^{-1}$; J. C. Pinkney & Nuker Team 2005) or ionized gas components ($\sigma \approx 459 \text{ km s}^{-1}$; Hypercat catalog). The ionized-gas velocity dispersion, in particular, appears to be unreliable. We compared our combined ALMA observations with SKYSAMPLER-based KinMS models adopting SMBH masses of $M_{\text{BH}} \approx 2.0 \times 10^9 M_{\odot}$ (from the stellar dispersion) and $M_{\text{BH}} \approx 1.2 \times 10^{10} M_{\odot}$ (from the ionized-gas dispersion). In these models, all other parame-

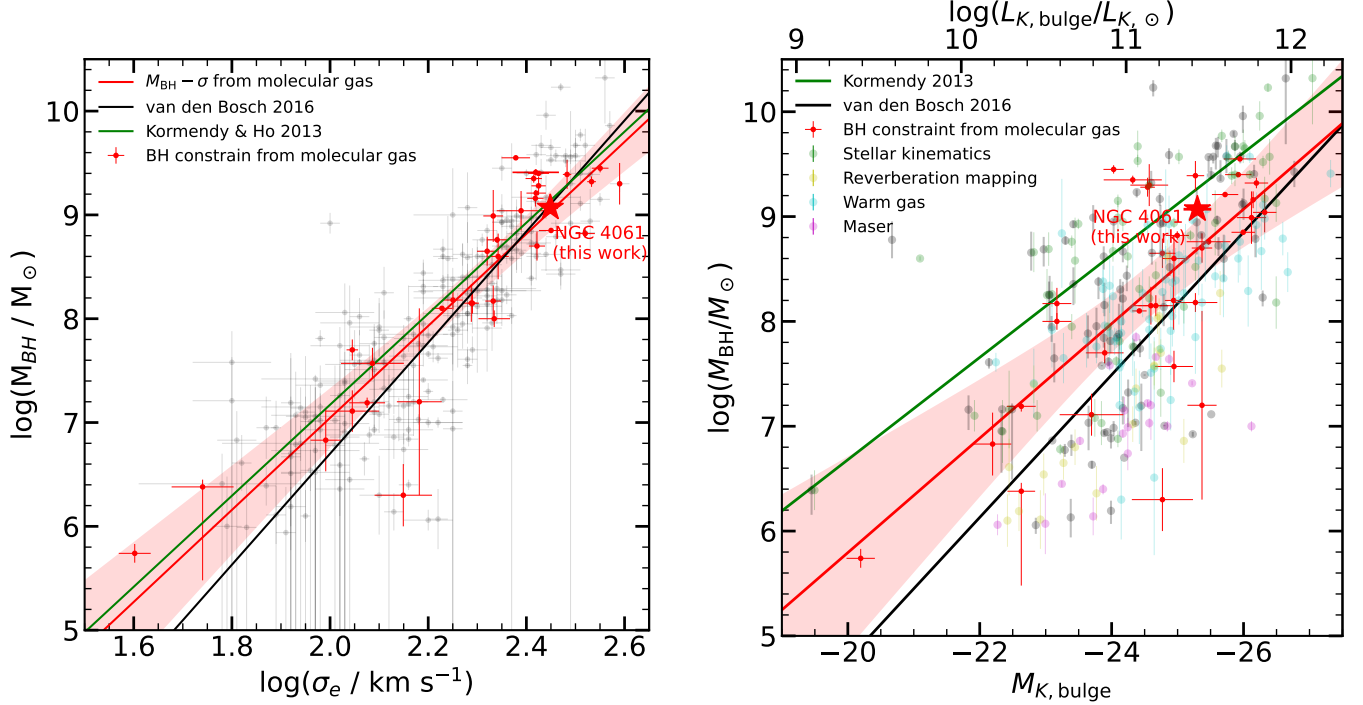


Figure 16. Our M_{BH} measurement for NGC 4061 is shown in comparison with both the well-established literature $M_{\text{BH}}-\sigma$ and $M_{\text{BH}}-L_{K,\text{bulge}}$ relations, as well as the molecular-gas-based relations alone, including their intrinsic scatters.

ters were fixed to the best-fit values listed in Table 8, while only M/L_{F814W} was allowed to vary to constrain the rotation of the outer $^{12}\text{CO}(2-1)$ CND. Figure 15 shows that neither model provides an adequate fit to the ALMA data. Although their favored M/L_{F814W} values decrease with increasing BH mass, both models systematically overpredict the rotation of the $^{12}\text{CO}(2-1)$ CND—either within the inner $0.^{\circ}6$ for $M_{\text{BH}} = 2.0 \times 10^9 \text{ M}_\odot$ or across the entire disk for $M_{\text{BH}} \approx 1.2 \times 10^{10} \text{ M}_\odot$. These results support our molecular-gas dynamical measurement and indicate that the SMBH mass in NGC 4061 is of order 10^9 M_\odot , at most slightly above one billion solar masses.

We also should note that a $\sim 10^9 \text{ M}_\odot$ SMBH at $\sim 107 \text{ Mpc}$ has an event-horizon angular size of only $\sim 0.4 \mu\text{as}$, far below the $\sim 10 \mu\text{as}$ reach of ngEHT (e.g., M. D. Johnson et al. 2023; A. Shlentsova et al. 2024), making direct horizon-scale imaging impossible at that distance.

4.7. NGC 4061 Positions on the Molecular Gas Alone $M_{\text{BH}}-\sigma$ and $M_{\text{BH}}-M_\star$ Scaling Relations

Our SMBH mass estimate for NGC 4061 is consistent within the $+1\sigma$ scatter of the $M_{\text{BH}}-\sigma$ relations compiled by R. C. E. van den Bosch (2016b) and J. Kormendy & L. C. Ho (2013), as shown in Figure 16. This agreement is expected, as both relations are calibrated primarily using classical bulges and elliptical galaxies, including brightest cluster galaxies, a category to which NGC 4061 belongs. The M_{BH} values predicted by these relations are $2.0 \times 10^9 \text{ M}_\odot$.

In contrast, on the $M_{\text{BH}}-L_{K,\text{bulge}}$ plane, our derived M_{BH} for NGC 4061 is consistent within -1σ of the compilation by J. Kormendy & L. C. Ho (2013), but lies nearly $+2\sigma$ above the relation presented by R. C. E. van den Bosch (2016b). This discrepancy likely reflects differences in the underlying datasets and measurement techniques adopted in the two compilations. Specifically, J. Kormendy & L. C. Ho (2013) included SMBH masses derived from stellar kinematics, ionized gas dynamics, and maser measurements, whereas R. C. E. van den Bosch (2016b) additionally incorporated reverberation-mapping estimates.

Over the past 12 years since the first successful molecular-gas-based M_{BH} measurement, obtained using Combined Array for Research in Millimeter-Wave Astronomy (CARMA) observations of NGC 4526 by T. A. Davis et al. (2013b), an additional 34 SMBH masses have been measured using ALMA. These molecular-gas-based measurements now span a mass range from 5×10^5 to $3.5 \times 10^9 \text{ M}_\odot$, including the measurement for NGC 4061 presented here. We summarize all 35 molecular-gas-based M_{BH} measurements in Table 10.

We then recompiled these scaling relations using only the 35 molecular-gas-based M_{BH} measurements by performing linear regression analyses with the LINREGRESS routine from the SciPy package (P. Virtanen et al. 2020). Galaxy K -band magnitudes were obtained from the HyperLeda database¹⁹.

¹⁹ <http://atlas.obs-hp.fr/hyperleda/>

Table 10. SMBH mass measurements derived solely from molecular gas dynamics. Here, σ_e denotes the stellar velocity dispersion within the galaxy's effective radius, and M_K is the absolute K -band magnitude obtained from the HyperLeda database. All quoted uncertainties correspond to the 1σ confidence level.

No.	Galaxy	$\log(M_{\text{BH}}/M_{\odot})$	σ_e (km s $^{-1}$)	$M_{K,\text{bulge}}$ (mag)	$\log(L_{K,\text{bulge}}/L_{\odot})$	References
(1)	(2)	(3)	(4)	(5)	(6)	(7)
1	Fairall 49	8.20 ± 0.28	—	-24.94 ± 0.13	11.29 ± 0.06	F. Lelli et al. (2022)
2	NGC 315	9.32 ± 0.05	341 ± 7	-26.19 ± 0.18	11.79 ± 0.08	B. D. Boizelle et al. (2021)
3	NGC 383	9.55 ± 0.02	239 ± 16	-25.94 ± 0.24	11.69 ± 0.11	E. V. North et al. (2019) H. Zhang et al. (2025)
4	NGC 404	5.74 ± 0.09	40 ± 3	-20.20 ± 0.22	9.39 ± 0.10	T. A. Davis et al. (2020)
5	NGC 524	8.60 ± 0.22	220 ± 11	-24.94 ± 0.18	11.29 ± 0.08	M. D. Smith et al. (2019, 2021)
6	NGC 613	7.57 ± 0.15	122 ± 18	-24.94 ± 0.29	11.29 ± 0.13	Combes, F. et al. (2019)
7	NGC 997	8.99 ± 0.25	215 ± 10	-26.12 ± 0.22	11.76 ± 0.10	P. Dominiak et al. (2024)
8	NGC 1097	8.15 ± 0.10	195 ± 4	-24.67 ± 0.26	11.18 ± 0.12	K. Onishi et al. (2015)
9	NGC 1275	9.04 ± 0.19	245 ± 28	-26.32 ± 0.18	11.84 ± 0.08	H. Nagai et al. (2019)
10	NGC 1326	7.11 ± 0.20	111 ± 14	-23.69 ± 0.48	10.79 ± 0.22	Combes, F. et al. (2019)
11	NGC 1332	8.82 ± 0.04	331 ± 15	-25.00 ± 0.18	11.31 ± 0.08	A. J. Barth et al. (2016)
12	NGC 1365	6.30 ± 0.30	141 ± 19	-24.77 ± 0.46	11.12 ± 0.12	Combes, F. et al. (2019)
13	NGC 1380	8.17 ± 0.15	215 ± 8	-23.17 ± 0.22	10.58 ± 0.10	K. M. Kabasares et al. (2022)
14	NGC 1566	6.83 ± 0.30	98 ± 7	-22.19 ± 0.28	10.19 ± 0.13	Combes, F. et al. (2019)
15	NGC 1574	8.00 ± 0.08	216 ± 16	-23.17 ± 0.22	10.58 ± 0.10	I. Ruffa et al. (2023)
16	NGC 1672	7.70 ± 0.10	111 ± 3	-23.89 ± 0.29	10.87 ± 0.13	Combes, F. et al. (2019)
17	NGC 1684	9.16 ± 0.08	262 ± 10	-26.14 ± 0.00	11.77 ± 0.10	P. Dominiak et al. (2024)
18	NGC 3258	9.35 ± 0.04	260 ± 10	-24.32 ± 0.44	11.04 ± 0.20	B. D. Boizelle et al. (2019)
19	NGC 3504	7.19 ± 0.05	119 ± 10	-22.63 ± 0.22	10.36 ± 0.10	D. D. Nguyen et al. (2020)
20	NGC 3557	8.85 ± 0.02	282 ± 16	-26.00 ± 0.18	11.71 ± 0.08	I. Ruffa et al. (2019)
21	NGC 3593	$6.38^{+0.08}_{-0.90}$	55 ± 7	-22.63 ± 0.22	10.36 ± 0.10	D. D. Nguyen et al. (2022)
22	NGC 3665	8.76 ± 0.03	219 ± 10	-25.47 ± 0.33	11.50 ± 0.15	K. Onishi et al. (2017)
23	NGC 4061	9.07 ± 0.04	$290 \pm \dots$	-25.27 ± 0.13	11.60 ± 0.09	This Work
24	NGC 4261	9.21 ± 0.01	263 ± 12	-25.72 ± 0.20	11.60 ± 0.09	I. Ruffa et al. (2023)
25	NGC 4429	8.18 ± 0.09	178 ± 8	-25.27 ± 0.33	11.42 ± 0.15	T. A. Davis et al. (2018)
26	NGC 4526	8.65 ± 0.14	209 ± 10	-24.77 ± 0.20	11.12 ± 0.09	T. A. Davis et al. (2013b)
27	NGC 4697	8.10 ± 0.02	169 ± 8	-24.42 ± 0.11	11.08 ± 0.05	T. A. Davis et al. (2017)
28	NGC 4751	9.45 ± 0.04	355 ± 14	-24.03 ± 0.15	10.92 ± 0.07	P. Dominiak et al. (2025)
29	NGC 4786	8.70 ± 0.14	264 ± 10	-25.37 ± 0.15	11.46 ± 0.07	K. M. Kabasares et al. (2024)
30	NGC 5193	8.15 ± 0.18	194 ± 7	-24.59 ± 0.26	11.15 ± 0.12	K. M. Kabasares et al. (2024)
31	NGC 6861	9.30 ± 0.20	389 ± 3	-24.57 ± 0.29	11.14 ± 0.13	K. M. Kabasares et al. (2022)
32	NGC 7052	9.40 ± 0.02	266 ± 13	-25.92 ± 0.20	11.68 ± 0.09	M. D. Smith et al. (2019, 2021)
33	NGC 7469	7.20 ± 0.90	152 ± 16	-25.37 ± 0.22	11.46 ± 0.10	H. N. Ngo et al. (2025)
34	PGC 11179	9.28 ± 0.09	266 ± 9	-24.55 ± 0.11	11.13 ± 0.05	D. D. Nguyen et al. (2021)
35	UGC 2698	9.39 ± 0.14	304 ± 6	-25.27 ± 0.13	11.42 ± 0.06	J. H. Cohn et al. (2023)

All regressions were performed in log–linear space, with all quantities converted to logarithmic units before fitting, and a flat prior for fitting parameters was also applied. The resulting best-fit relations, including the 95% confidence-level uncertainties, shown as red lines in Figure 16, yield

$$\log\left(\frac{M_{\text{BH}}}{M_{\odot}}\right) = -(1.25 \pm 0.94) + (4.20 \pm 0.38) \log\left(\frac{\sigma_e}{\text{km s}^{-1}}\right),$$

and

$$\log\left(\frac{M_{\text{BH}}}{M_{\odot}}\right) = -(4.46 \pm 0.30) - (0.52 \pm 0.09) \times M_{K,\text{bulge}}$$

The molecular-gas-constrained $M_{\text{BH}}-\sigma$ relation appears broadly consistent with the relation presented by [J. Kormendy & L. C. Ho \(2013\)](#), differing only by a small, approximately constant negative offset in M_{BH} (≈ 0.1 dex). Be-

cause molecular-gas-based measurements rely on dynamically cold, well-settled CNDs, which are relatively insensitive to inflows, outflows, and dark matter contributions on these scales, the resulting M_{BH} estimates are arguably more robust. The presence of only a small systematic offset likely reflects differences in modeling assumptions, thereby underscoring the overall consistency and reliability of the dynamical measurement techniques. In contrast, the discrepancy with the [R. C. E. van den Bosch \(2016b\)](#) relation can be attributed to the inclusion of the intrinsically less precise reverberation-mapping mass estimates in that compilation.

The molecular-gas-based $M_{\text{BH}}-L_{K,\text{bulge}}$ relation derived in this work exhibits a slope that is closely aligned with that of the relation compiled by [J. Kormendy & L. C. Ho \(2013\)](#), resulting in two nearly parallel relations with a modest offset in normalization. This similarity suggests that the underlying scaling between M_{BH} and bulge stellar mass is robust when restricted to samples dominated by classical bulges and early-type galaxies and calibrated using direct dynamical measurements. In contrast, the relation presented by [R. C. E. van den Bosch \(2016b\)](#) exhibits a noticeably different slope, likely reflecting the broader, more heterogeneous nature of their sample, which includes a substantial fraction of SMBH masses derived from reverberation mapping. The inclusion of indirect mass estimators, combined with differences in galaxy morphology and regression methodology, can modify both the slope and normalization of the resulting scaling relation, thereby accounting for the observed divergence relative to the purely dynamical and molecular-gas-based relations.

5. CONCLUSIONS

We derive the first dynamical SMBH mass in NGC 4061 through dynamical modeling of cold molecular gas, using ALMA $^{12}\text{CO}(2-1)$ observations that combine medium-angular-resolution data from Cycle 7 ($\theta_{\text{beam}} \approx 0''.32 \times 0''.24$) with higher-resolution archival data from Cycle 6 ($\theta_{\text{beam}} \approx 0''.11 \times 0''.12$). The resulting data set attains a synthesized beam of $0''.16 \times 0''.13$, corresponding to $83.2 \times 67.6 \text{ pc}^2$, which closely matches the estimated SOI radius of the SMBH ($r_{\text{soi}} \approx 0''.12$). By exploring multiple prescriptions for the spatial distribution of the molecular gas in the $^{12}\text{CO}(2-1)$ CND, we obtain consistent constraints on the black hole mass, the stellar mass-to-light ratio, and other disk parameters. These models yield a robust dynamical mea-

surement of $M_{\text{BH}} = (1.17^{+0.08}_{-0.10} \text{ [stat.]} \pm 0.43 \text{ [syst.]}) \times 10^9 M_{\odot}$ and an I -band stellar mass-to-light ratio of $M/L_{\text{F814W}} = 3.46^{+0.07}_{-0.06} \text{ [stat.]} \pm 0.10 \text{ [syst.] } M_{\odot}/L_{\odot}$. Our results highlight the importance of high-spatial-resolution ALMA observations of cold molecular gas for precision SMBH mass measurements. Provided that the synthesized beam remains comparable to the BH's SOI, $^{12}\text{CO}(2-1)$ serves as a reliable dynamical tracer, in contrast to warm ionized gas, which is frequently affected by non-circular motions and other dynamical disturbances.

Our results conclusively resolve the long-standing discrepancy among previous indirect M_{BH} -estimates for NGC 4061, arising from inconsistent stellar velocity dispersion measurements, and demonstrate that the exceptionally large dispersion reported in the literature is likely incorrect.

The $M_{\text{BH}}-\sigma$ and $M_{\text{BH}}-L_{K,\text{bulge}}$ relations derived from molecular-gas-based measurements alone are consistent with the relations of [J. Kormendy & L. C. Ho \(2013\)](#), but not with those of [R. C. E. van den Bosch \(2016b\)](#). This likely reflects the use of direct dynamical SMBH mass measurements in the former, compared to the inclusion of reverberation-mapping estimates and a more heterogeneous sample in the latter.

ACKNOWLEDGEMENTS

This paper makes use of the following ALMA data: ADS/JAO.ALMA#2018.1.00397.S and #2019.1.00036.S. ALMA is a partnership of ESO (representing its member states), NSF (USA), and NINS (Japan), together with NRC (Canada) and NSC and ASIAA (Taiwan), and KASI (Republic of Korea), in cooperation with the Republic of Chile. The Joint ALMA Observatory is operated by ESO, AUI/NRAO, and NAOJ. The National Radio Astronomy Observatory is a facility of the National Science Foundation operated under cooperative agreement by Associated Universities, Inc.

Facility: ALMA and *HST*/WFPC2

Software: Python 3.12 ([G. Van Rossum & F. L. Drake 2009](#)), Matplotlib 3.6 ([J. D. Hunter 2007](#)), NumPy 1.22 ([C. R. Harris et al. 2020](#)), SciPy 1.3 ([P. Virtanen et al. 2020](#)), photutils 0.7 ([L. Bradley et al. 2024](#)), AstroPy 5.1 ([Astropy Collaboration et al. 2022](#)), AdaMet 2.0 ([M. Cappellari et al. 2013a](#)), JamPy 7.2 ([M. Cappellari 2020](#)), and MgeFit 5.0 ([M. Cappellari 2002b](#)).

REFERENCES

Ahn, C. P., Seth, A. C., Cappellari, M., et al. 2018, *ApJ*, 858, 102, doi: [10.3847/1538-4357/aabc57](https://doi.org/10.3847/1538-4357/aabc57)

Astropy Collaboration, Price-Whelan, A. M., Lim, P. L., et al. 2022, *ApJ*, 935, 167, doi: [10.3847/1538-4357/ac7c74](https://doi.org/10.3847/1538-4357/ac7c74)

Avila, R. J., Hack, W. J., & STScI AstroDrizzle Team. 2012, in American Astronomical Society Meeting Abstracts, Vol. 220, American Astronomical Society Meeting Abstracts #220, 135.13

Baldassare, V. F., Reines, A. E., Gallo, E., & Greene, J. E. 2015, *ApJL*, 809, L14, doi: [10.1088/2041-8205/809/1/L14](https://doi.org/10.1088/2041-8205/809/1/L14)

Barth, A. J., Boizelle, B. D., Darling, J., et al. 2016, *ApJL*, 822, L28, doi: [10.3847/2041-8205/822/2/L28](https://doi.org/10.3847/2041-8205/822/2/L28)

Bertin, E., & Arnouts, S. 1996, *A&AS*, 117, 393, doi: [10.1051/aas:1996164](https://doi.org/10.1051/aas:1996164)

Boizelle, B. D., Barth, A. J., Walsh, J. L., et al. 2019, *ApJ*, 881, 10, doi: [10.3847/1538-4357/ab2a0a](https://doi.org/10.3847/1538-4357/ab2a0a)

Boizelle, B. D., Walsh, J. L., Barth, A. J., et al. 2021, *ApJ*, 908, 19, doi: [10.3847/1538-4357/abd24d](https://doi.org/10.3847/1538-4357/abd24d)

Bolatto, A. D., Wolfire, M., & Leroy, A. K. 2013, *ARA&A*, 51, 207, doi: [10.1146/annurev-astro-082812-140944](https://doi.org/10.1146/annurev-astro-082812-140944)

Bradley, L., Sipőcz, B., Robitaille, T., et al. 2024, 2.0.2 Zenodo, doi: [10.5281/zenodo.13989456](https://doi.org/10.5281/zenodo.13989456)

Cappellari, M. 2002a, *MNRAS*, 333, 400, doi: [10.1046/j.1365-8711.2002.05412.x](https://doi.org/10.1046/j.1365-8711.2002.05412.x)

Cappellari, M. 2002b, *MNRAS*, 333, 400, doi: [10.1046/j.1365-8711.2002.05412.x](https://doi.org/10.1046/j.1365-8711.2002.05412.x)

Cappellari, M. 2008, *MNRAS*, 390, 71, doi: [10.1111/j.1365-2966.2008.13754.x](https://doi.org/10.1111/j.1365-2966.2008.13754.x)

Cappellari, M. 2016, *ARA&A*, 54, 597, doi: [10.1146/annurev-astro-082214-122432](https://doi.org/10.1146/annurev-astro-082214-122432)

Cappellari, M. 2020, *MNRAS*, 494, 4819, doi: [10.1093/mnras/staa959](https://doi.org/10.1093/mnras/staa959)

Cappellari, M., Scott, N., Alatalo, K., et al. 2013a, *MNRAS*, 432, 1709, doi: [10.1093/mnras/stt562](https://doi.org/10.1093/mnras/stt562)

Cappellari, M., Scott, N., Alatalo, K., et al. 2013b, *MNRAS*, 432, 1709, doi: [10.1093/mnras/stt562](https://doi.org/10.1093/mnras/stt562)

Cohn, J. H., Walsh, J. L., Boizelle, B. D., et al. 2021, *ApJ*, 919, 77, doi: [10.3847/1538-4357/ac0f78](https://doi.org/10.3847/1538-4357/ac0f78)

Cohn, J. H., Curliss, M., Walsh, J. L., et al. 2023, *ApJ*, 958, 186, doi: [10.3847/1538-4357/ad029d](https://doi.org/10.3847/1538-4357/ad029d)

Combes, F., García-Burillo, S., Audibert, A., et al. 2019, *A&A*, 623, A79, doi: [10.1051/0004-6361/201834560](https://doi.org/10.1051/0004-6361/201834560)

Dame, T. M. 2011, arXiv e-prints, arXiv:1101.1499, <https://arxiv.org/abs/1101.1499>

Davis, T. A. 2014, *MNRAS*, 443, 911, doi: [10.1093/mnras/stu1163](https://doi.org/10.1093/mnras/stu1163)

Davis, T. A., Bureau, M., Cappellari, M., Sarzi, M., & Blitz, L. 2013a, *Nature*, 494, 328, doi: [10.1038/nature11819](https://doi.org/10.1038/nature11819)

Davis, T. A., Bureau, M., Cappellari, M., Sarzi, M., & Blitz, L. 2013b, *Nature*, 494, 328, doi: [10.1038/nature11819](https://doi.org/10.1038/nature11819)

Davis, T. A., Bureau, M., Onishi, K., et al. 2017, *MNRAS*, 468, 4675, doi: [10.1093/mnras/stw3217](https://doi.org/10.1093/mnras/stw3217)

Davis, T. A., Bureau, M., Onishi, K., et al. 2018, *MNRAS*, 473, 3818, doi: [10.1093/mnras/stx2600](https://doi.org/10.1093/mnras/stx2600)

Davis, T. A., Nguyen, D. D., Seth, A. C., et al. 2020, *MNRAS*, 496, 4061, doi: [10.1093/mnras/staa1567](https://doi.org/10.1093/mnras/staa1567)

den Brok, M., Seth, A. C., Barth, A. J., et al. 2015, *ApJ*, 809, 101, doi: [10.1088/0004-637X/809/1/101](https://doi.org/10.1088/0004-637X/809/1/101)

Doe, S. M., Ledlow, M. J., Burns, J. O., & White, R. A. 1995, *AJ*, 110, 46, doi: [10.1086/117496](https://doi.org/10.1086/117496)

Dominiak, P., Bureau, M., Davis, T. A., et al. 2024, *Monthly Notices of the Royal Astronomical Society*, 529, 1597, doi: [10.1093/mnras/stae314](https://doi.org/10.1093/mnras/stae314)

Dominiak, P., Cappellari, M., Bureau, M., et al. 2025, *Monthly Notices of the Royal Astronomical Society*, 542, 2039, doi: [10.1093/mnras/staf1338](https://doi.org/10.1093/mnras/staf1338)

Emsellem, E., Monnet, G., & Bacon, R. 1994, *A&A*, 285, 723

Fabian, A. C. 2012, *ARA&A*, 50, 455, doi: [10.1146/annurev-astro-081811-125521](https://doi.org/10.1146/annurev-astro-081811-125521)

Ferrarese, L., & Merritt, D. 2000, *ApJL*, 539, L9, doi: [10.1086/312838](https://doi.org/10.1086/312838)

Freeland, E., Sengupta, C., & Croston, J. H. 2010, *MNRAS*, 409, 1518, doi: [10.1111/j.1365-2966.2010.17379.x](https://doi.org/10.1111/j.1365-2966.2010.17379.x)

Graham, A. W., Chilingarian, I., Nguyen, D. D., et al. 2025, *PASA*, 42, e068, doi: [10.1017/pasa.2025.10035](https://doi.org/10.1017/pasa.2025.10035)

Graham, A. W., & Scott, N. 2013, *ApJ*, 764, 151, doi: [10.1088/0004-637X/764/2/151](https://doi.org/10.1088/0004-637X/764/2/151)

Greene, J. E., Strader, J., & Ho, L. C. 2020a, *ARA&A*, 58, 257, doi: [10.1146/annurev-astro-032620-021835](https://doi.org/10.1146/annurev-astro-032620-021835)

Greene, J. E., Strader, J., & Ho, L. C. 2020b, *ARA&A*, 58, 257, doi: [10.1146/annurev-astro-032620-021835](https://doi.org/10.1146/annurev-astro-032620-021835)

Greene, J. E., Labbe, I., Goulding, A. D., et al. 2024, *ApJ*, 964, 39, doi: [10.3847/1538-4357/ad1e5f](https://doi.org/10.3847/1538-4357/ad1e5f)

Haario, H., Saksman, E., & Tamminen, J. 2001, *Bernoulli*, 7, 223

Harris, C. R., Millman, K. J., van der Walt, S. J., et al. 2020, *Nature*, 585, 357, doi: [10.1038/s41586-020-2649-2](https://doi.org/10.1038/s41586-020-2649-2)

Hlavacek-Larrondo, J., Fabian, A. C., Edge, A. C., & Hogan, M. T. 2012, *MNRAS*, 424, 224, doi: [10.1111/j.1365-2966.2012.21187.x](https://doi.org/10.1111/j.1365-2966.2012.21187.x)

Högblom, J. A. 1974, *A&AS*, 15, 417

Hunter, J. D. 2007, *Computing In Science & Engineering*, 9, 90, doi: [10.1109/MCSE.2007.55](https://doi.org/10.1109/MCSE.2007.55)

Inayoshi, K., Visbal, E., & Haiman, Z. 2020, *ARA&A*, 58, 27, doi: [10.1146/annurev-astro-120419-014455](https://doi.org/10.1146/annurev-astro-120419-014455)

Johnson, M. D., Doeleman, S. S., Gómez, J. L., & Broderick, A. E. 2023, *Galaxies*, 11, 92, doi: [10.3390/galaxies11050092](https://doi.org/10.3390/galaxies11050092)

Kabasares, K. M., Barth, A. J., Buote, D. A., et al. 2022, *The Astrophysical Journal*, 934, 162, doi: [10.3847/1538-4357/ac7a38](https://doi.org/10.3847/1538-4357/ac7a38)

Kabasares, K. M., Cohn, J. H., Barth, A. J., et al. 2024, *The Astrophysical Journal*, 966, 132, doi: [10.3847/1538-4357/ad2f36](https://doi.org/10.3847/1538-4357/ad2f36)

Kelley, L. Z. 2025, arXiv e-prints, arXiv:2505.00797, doi: [10.48550/arXiv.2505.00797](https://doi.org/10.48550/arXiv.2505.00797)

Keppler, M., Teague, R., Bae, J., et al. 2019, *A&A*, 625, A118, doi: [10.1051/0004-6361/201935034](https://doi.org/10.1051/0004-6361/201935034)

Kormendy, J., & Ho, L. C. 2013, *ARA&A*, 51, 511, doi: [10.1146/annurev-astro-082708-101811](https://doi.org/10.1146/annurev-astro-082708-101811)

Krajnović, D., Cappellari, M., & McDermid, R. M. 2018, *MNRAS*, 473, 5237, doi: [10.1093/mnras/stx2704](https://doi.org/10.1093/mnras/stx2704)

Krist, J. E., Hook, R. N., & Stoehr, F. 2011, in Society of Photo-Optical Instrumentation Engineers (SPIE) Conference Series, Vol. 8127, Optical Modeling and Performance Predictions V, ed. M. A. Kahan, 81270J, doi: [10.1117/12.892762](https://doi.org/10.1117/12.892762)

Lelli, F., Davis, T. A., Bureau, M., et al. 2022, Monthly Notices of the Royal Astronomical Society, 516, 4066, doi: [10.1093/mnras/stac2493](https://doi.org/10.1093/mnras/stac2493)

Ma, C.-P., Greene, J. E., McConnell, N., et al. 2014, ApJ, 795, 158, doi: [10.1088/0004-637X/795/2/158](https://doi.org/10.1088/0004-637X/795/2/158)

Magorrian, J., Tremaine, S., Richstone, D., et al. 1998, AJ, 115, 2285, doi: [10.1086/300353](https://doi.org/10.1086/300353)

McConnell, N. J., & Ma, C.-P. 2013, ApJ, 764, 184, doi: [10.1088/0004-637X/764/2/184](https://doi.org/10.1088/0004-637X/764/2/184)

McConnell, N. J., Ma, C.-P., Gebhardt, K., et al. 2011, Nature, 480, 215, doi: [10.1038/nature10636](https://doi.org/10.1038/nature10636)

McConnell, N. J., Ma, C.-P., Murphy, J. D., et al. 2012, ApJ, 756, 179, doi: [10.1088/0004-637X/756/2/179](https://doi.org/10.1088/0004-637X/756/2/179)

McMullin, J. P., Waters, B., Schiebel, D., Young, W., & Golap, K. 2007, in Astronomical Society of the Pacific Conference Series, Vol. 376, Astronomical Data Analysis Software and Systems XVI, ed. R. A. Shaw, F. Hill, & D. J. Bell, 127

Mehrgan, K., Thomas, J., Saglia, R., et al. 2019, ApJ, 887, 195, doi: [10.3847/1538-4357/ab5856](https://doi.org/10.3847/1538-4357/ab5856)

Melo-Carneiro, C. R., Collett, T. E., Oldham, L. J., et al. 2025, MNRAS, 541, 2853, doi: [10.1093/mnras/staf1036](https://doi.org/10.1093/mnras/staf1036)

Mitzkus, M., Cappellari, M., & Walcher, C. J. 2017, MNRAS, 464, 4789, doi: [10.1093/mnras/stw2677](https://doi.org/10.1093/mnras/stw2677)

Naab, T., & Ostriker, J. P. 2017, ARA&A, 55, 59, doi: [10.1146/annurev-astro-081913-040019](https://doi.org/10.1146/annurev-astro-081913-040019)

Nagai, H., Onishi, K., Kawakatu, N., et al. 2019, ApJ, 883, 193, doi: [10.3847/1538-4357/ab3e6e](https://doi.org/10.3847/1538-4357/ab3e6e)

Netzer, H. 2015, ARA&A, 53, 365, doi: [10.1146/annurev-astro-082214-122302](https://doi.org/10.1146/annurev-astro-082214-122302)

Ngo, H. N., Nguyen, D. D., Le, T. Q. T., et al. 2025, ApJ, 992, 211, doi: [10.3847/1538-4357/ae0455](https://doi.org/10.3847/1538-4357/ae0455)

Nguyen, D. D. 2017, arXiv e-prints, arXiv:1712.02470, doi: [10.48550/arXiv.1712.02470](https://doi.org/10.48550/arXiv.1712.02470)

Nguyen, D. D. 2019, in ALMA2019: Science Results and Cross-Facility Synergies, 106, doi: [10.5281/zenodo.3585410](https://doi.org/10.5281/zenodo.3585410)

Nguyen, D. D., Cappellari, M., & Pereira-Santalla, M. 2023, MNRAS, 526, 3548, doi: [10.1093/mnras/stad2860](https://doi.org/10.1093/mnras/stad2860)

Nguyen, D. D., Seth, A. C., Reines, A. E., et al. 2014, ApJ, 794, 34, doi: [10.1088/0004-637X/794/1/34](https://doi.org/10.1088/0004-637X/794/1/34)

Nguyen, D. D., Seth, A. C., den Brok, M., et al. 2017, ApJ, 836, 237, doi: [10.3847/1538-4357/aa5cb4](https://doi.org/10.3847/1538-4357/aa5cb4)

Nguyen, D. D., Seth, A. C., Neumayer, N., et al. 2018, ApJ, 858, 118, doi: [10.3847/1538-4357/aabe28](https://doi.org/10.3847/1538-4357/aabe28)

Nguyen, D. D., Seth, A. C., Neumayer, N., et al. 2019, ApJ, 872, 104, doi: [10.3847/1538-4357/aafe7a](https://doi.org/10.3847/1538-4357/aafe7a)

Nguyen, D. D., den Brok, M., Seth, A. C., et al. 2020, ApJ, 892, 68, doi: [10.3847/1538-4357/ab77aa](https://doi.org/10.3847/1538-4357/ab77aa)

Nguyen, D. D., Izumi, T., Thater, S., et al. 2021, MNRAS, 504, 4123, doi: [10.1093/mnras/stab1002](https://doi.org/10.1093/mnras/stab1002)

Nguyen, D. D., Bureau, M., Thater, S., et al. 2022, MNRAS, 509, 2920, doi: [10.1093/mnras/stab3016](https://doi.org/10.1093/mnras/stab3016)

Nguyen, D. D., Cappellari, M., Ngo, H. N., et al. 2025a, AJ, 170, 124, doi: [10.3847/1538-3881/ade9ba](https://doi.org/10.3847/1538-3881/ade9ba)

Nguyen, D. D., Cappellari, M., Le, T. Q. T., et al. 2025b, arXiv e-prints, arXiv:2511.10427. <https://arxiv.org/abs/2511.10427>

Nguyen, D. D., Ngo, H. N., Cappellari, M., et al. 2025c, arXiv e-prints, arXiv:2509.20519. <https://arxiv.org/abs/2509.20519>

Nguyen, D. D., Le, T. N., Cappellari, M., et al. 2026, arXiv e-prints, arXiv:2601.17439. <https://arxiv.org/abs/2601.17439>

Nightingale, J. W., Smith, R. J., He, Q., et al. 2023, MNRAS, 521, 3298, doi: [10.1093/mnras/stad587](https://doi.org/10.1093/mnras/stad587)

North, E. V., Davis, T. A., Bureau, M., et al. 2019, MNRAS, 490, 319, doi: [10.1093/mnras/stz2598](https://doi.org/10.1093/mnras/stz2598)

Onishi, K., Iguchi, S., Davis, T. A., et al. 2017, MNRAS, 468, 4663, doi: [10.1093/mnras/stx631](https://doi.org/10.1093/mnras/stx631)

Onishi, K., Iguchi, S., Sheth, K., & Kohno, K. 2015, ApJ, 806, 39, doi: [10.1088/0004-637X/806/1/39](https://doi.org/10.1088/0004-637X/806/1/39)

Pacucci, F., Nguyen, B., Carniani, S., Maiolino, R., & Fan, X. 2023, ApJL, 957, L3, doi: [10.3847/2041-8213/ad0158](https://doi.org/10.3847/2041-8213/ad0158)

Pinkney, J. C., & Nuker Team. 2005, in American Astronomical Society Meeting Abstracts, Vol. 206, American Astronomical Society Meeting Abstracts #206, 11.17

Postiglione, J., Ford, K. E. S., Best, H., McKernan, B., & O'Dowd, M. 2025, ApJ, 991, 161, doi: [10.3847/1538-4357/adfa0c](https://doi.org/10.3847/1538-4357/adfa0c)

Rau, U., & Cornwell, T. J. 2011, A&A, 532, A71, doi: [10.1051/0004-6361/201117104](https://doi.org/10.1051/0004-6361/201117104)

Reines, A. E., Greene, J. E., & Geha, M. 2013, ApJ, 775, 116, doi: [10.1088/0004-637X/775/2/116](https://doi.org/10.1088/0004-637X/775/2/116)

Ruffa, I., Davis, T. A., Prandoni, I., et al. 2019, MNRAS, 489, 3739, doi: [10.1093/mnras/stz2368](https://doi.org/10.1093/mnras/stz2368)

Ruffa, I., Davis, T. A., Cappellari, M., et al. 2023, MNRAS, 522, 6170, doi: [10.1093/mnras/stad1119](https://doi.org/10.1093/mnras/stad1119)

Rushi, S. P., Erwin, P., Saglia, R. P., et al. 2013a, AJ, 146, 160, doi: [10.1088/0004-6256/146/6/160](https://doi.org/10.1088/0004-6256/146/6/160)

Rushi, S. P., Thomas, J., Saglia, R. P., et al. 2013b, AJ, 146, 45, doi: [10.1088/0004-6256/146/3/45](https://doi.org/10.1088/0004-6256/146/3/45)

Saglia, R. P., Opitsch, M., Erwin, P., et al. 2016, ApJ, 818, 47, doi: [10.3847/0004-637X/818/1/47](https://doi.org/10.3847/0004-637X/818/1/47)

Seth, A. C., van den Bosch, R., Mieske, S., et al. 2014, Nature, 513, 398, doi: [10.1038/nature13762](https://doi.org/10.1038/nature13762)

Shlentsova, A., Roelofs, F., Issaoun, S., Davelaar, J., & Falcke, H. 2024, A&A, 686, A154, doi: [10.1051/0004-6361/202347214](https://doi.org/10.1051/0004-6361/202347214)

Silk, J., & Rees, M. J. 1998, A&A, 331, L1, doi: [10.48550/arXiv.astro-ph/9801013](https://doi.org/10.48550/arXiv.astro-ph/9801013)

Smith, M. D., Bureau, M., Davis, T. A., et al. 2019, MNRAS, 485, 4359, doi: [10.1093/mnras/stz625](https://doi.org/10.1093/mnras/stz625)

Smith, M. D., Bureau, M., Davis, T. A., et al. 2021, MNRAS, 503, 5984, doi: [10.1093/mnras/stab791](https://doi.org/10.1093/mnras/stab791)

Taylor, M. A., Tahmasebzadeh, B., Thompson, S., et al. 2025, ApJL, 991, L24, doi: [10.3847/2041-8213/ae028e](https://doi.org/10.3847/2041-8213/ae028e)

Thater, S., Lyubenova, M., Fahrion, K., et al. 2023, A&A, 675, A18, doi: [10.1051/0004-6361/202245362](https://doi.org/10.1051/0004-6361/202245362)

Thater, S., Krajnović, D., Weilbacher, P. M., et al. 2022, MNRAS, 509, 5416, doi: [10.1093/mnras/stab3210](https://doi.org/10.1093/mnras/stab3210)

Thomas, J., Ma, C.-P., McConnell, N. J., et al. 2016, Nature, 532, 340, doi: [10.1038/nature17197](https://doi.org/10.1038/nature17197)

van den Bosch, R. C. E. 2016a, ApJ, 831, 134, doi: [10.3847/0004-637X/831/2/134](https://doi.org/10.3847/0004-637X/831/2/134)

van den Bosch, R. C. E. 2016b, ApJ, 831, 134, doi: [10.3847/0004-637X/831/2/134](https://doi.org/10.3847/0004-637X/831/2/134)

van den Bosch, R. C. E., & van de Ven, G. 2009, MNRAS, 398, 1117, doi: [10.1111/j.1365-2966.2009.15177.x](https://doi.org/10.1111/j.1365-2966.2009.15177.x)

Van Rossum, G., & Drake, F. L. 2009, Python 3 Reference Manual (Scotts Valley, CA: CreateSpace)

Virtanen, P., Gommers, R., Oliphant, T. E., et al. 2020, Nature Methods, 17, 261, doi: [10.1038/s41592-019-0686-2](https://doi.org/10.1038/s41592-019-0686-2)

Voggel, K. T., Seth, A. C., Neumayer, N., et al. 2018, ApJ, 858, 20, doi: [10.3847/1538-4357/aabae5](https://doi.org/10.3847/1538-4357/aabae5)

Willmer, C. N. A. 2018, ApJS, 236, 47, doi: [10.3847/1538-4365/aabfdf](https://doi.org/10.3847/1538-4365/aabfdf)

Zhang, H., Bureau, M., Ruffa, I., et al. 2025, Monthly Notices of the Royal Astronomical Society, 537, 520, doi: [10.1093/mnras/staf055](https://doi.org/10.1093/mnras/staf055)